

Theory of electron spin resonance in scanning tunneling microscopy

Christian R. Ast ^{1,*}, Piotr Kot ¹, Maneesha Ismail ¹, Sebastián de-la-Peña ²,
Antonio I. Fernández-Domínguez ² and Juan Carlos Cuevas ²

¹Max-Planck-Institut für Festkörperforschung, Heisenbergstraße 1, 70569 Stuttgart, Germany

²Departamento de Física Teórica de la Materia Condensada and Condensed Matter Physics Center (IFIMAC),
Universidad Autónoma de Madrid, 28049 Madrid, Spain



(Received 17 September 2023; accepted 1 April 2024; published 6 May 2024)

Electron spin resonance (ESR) spectroscopy in scanning tunneling microscopy (STM) has enabled probing the electronic structure of single magnetic atoms and molecules on surfaces with unprecedented energy resolution, as well as demonstrating coherent manipulation of single spins. Despite this remarkable success, the field could still be greatly advanced by a more quantitative understanding of the ESR-STM physical mechanisms. Here, we present a theory of ESR-STM that quantitatively models not only the ESR signal itself, but also the full background tunneling current, from which the ESR signal is derived. Our theory is based on a combination of Green's function techniques to describe the electron tunneling and a quantum master equation for the dynamics of the spin system along with microwave radiation interacting with both the tunneling current and the magnetic system. We show that this theory is able to quantitatively reproduce the experimental results for a spin-1/2 system (TiH molecules on MgO) across many orders of magnitude in tunneling current, providing access to the relaxation and decoherence rates that govern the spin dynamics due to intrinsic mechanisms and to the applied bias voltage. More importantly, our work establishes that (i) sizable ESR signals, which are a measure of microwave-induced changes in the junction magnetoresistance, require surprisingly high tip spin polarizations, and (ii) the coupling of the magnetization dynamics to the microwave field gives rise to the asymmetric ESR spectra often observed in this spectroscopy. Additionally, our theory provides very specific predictions for the dependence of the relaxation and decoherence times on the bias voltage and the tip-sample distance. Finally, with the help of electromagnetic simulations, we find that the transitions in our ESR-STM experiments, in which the tunnel junction is irradiated by a nearby microwave antenna, can be driven by the ac magnetic field at the junction.

DOI: [10.1103/PhysRevResearch.6.023126](https://doi.org/10.1103/PhysRevResearch.6.023126)

I. INTRODUCTION

Electron spin resonance (ESR), also referred to as electron paramagnetic resonance, is a widely used spectroscopy and imaging technique in chemistry, biology, and condensed matter physics to characterize systems with unpaired electrons [1]. The main advantage of ESR is its high-energy resolution, only limited by the decoherence time of magnetic excitations, while its spatial resolution is limited by the magnetic field gradients that can be implemented (resulting in a resolution of the order of $100 \mu\text{m}^3$ [2]). In 2015, Baumann and coworkers reported the first convincing implementation of ESR in the context of scanning tunneling microscopy (STM) by addressing single magnetic atoms on a surface using an oscillating electric field (20–30 GHz) [3]. In ESR-STM, the lifting of the spin degeneracy by means of an external magnetic field and the spin excitation through an external microwave source is

done in analogy to conventional ESR. The detection of the spin state, however, is realized through the measurement of the tunneling current in an appropriately spin-polarized tip, which ensures atomic scale spatial resolution, and is particular to STM. This is schematically shown in Fig. 1(a). Since the first demonstration, many different groups have reported experimental ESR-STM studies [4–22]. Thus, for instance, ESR-STM has been used to measure the hyperfine interaction in Ti atoms on a MgO surface [7], to achieve the coherent spin manipulation of individual atoms on a surface [13], to do magnetic resonance imaging of single atoms on a surface [11], to demonstrate the electric control of spin transitions at the atomic scale [21], and to do basic quantum computing operations with single atoms on a surface [22].

However, the physical mechanisms underlying ESR-STM are still under debate, for example, what drives the transitions between the magnetic states in an all-electric ESR-STM experiment. Many different mechanisms have been suggested [3,14,23–27], but there is no real consensus on this issue (for a detailed account of this debate, see Ref. [28]). Further points that need more clarification include, but are not limited to, what constitutes a suitable tip for acquiring ESR signals [11,29,30], how to extract relaxation and decoherence times of the spin excitations from continuous mode ESR spectra,

*Corresponding author: c.ast@fkf.mpg.de

Published by the American Physical Society under the terms of the [Creative Commons Attribution 4.0 International license](https://creativecommons.org/licenses/by/4.0/). Further distribution of this work must maintain attribution to the author(s) and the published article's title, journal citation, and DOI. Open access publication funded by Max Planck Society.

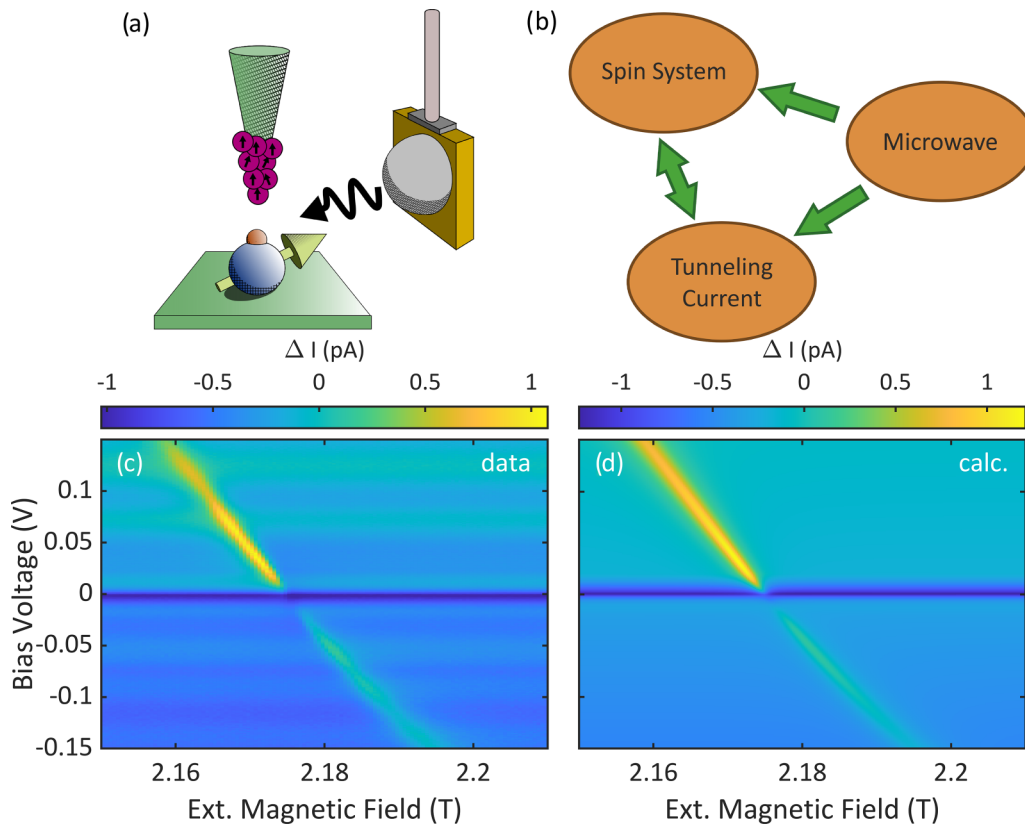


FIG. 1. Modeling the ESR-STM data. (a) Schematic drawing of the ESR tunnel junction. The microwave is supplied from an antenna radiating into the vacuum towards the tunnel junction. (b) The tunneling current and the spin system influence each other, while both interact with the microwave. The tunneling current in our theory is modeled by nonequilibrium Green's functions and the spin system dynamics is described by a master equation to calculate the density matrix. (c) Measured ESR signal as function of bias voltage and magnetic field at constant microwave frequency (61 GHz) in TiH molecules on MgO. (d) Calculated ESR signal using parameters fitted to the experimental data in (c) and the theory presented in this work.

how the bias voltage influences the ESR mechanism, and why some ESR signals are more asymmetric than others. Also, the role of the substrate is still poorly understood and most of the experiments have been done in the same type of substrate (MgO), although other substrates (NaCl) have been successfully explored recently [31]. To address these questions, it would be highly desirable to have an ESR-STM theory able to quantitatively reproduce the measured signals. The goal of this work is to provide such a theory and answer many of these open questions.

Part of the problem in developing an ESR-STM theory is that the interaction of the tunneling current with the spin system does not just probe the spin state, but also has a strong back-action on the dynamics of the spin state itself [32–34]. In ESR-STM, the microwaves introduce an additional component that interacts both with the spin system as well as the tunneling current. The complex interplay between the spin system, the tunneling current and the microwave is schematically shown in Fig. 1(b). Thus a quantitative understanding of the tunneling current has to take these three components into account along with their interactions. Here, we present a theory that quantitatively describes ESR-STM spectra. Our theory is based on a combination of nonequilibrium Green's function techniques for the calculation of the tunneling current and quantum master equations for the description of

the spin dynamics of the magnetic system. This theory takes into account the role of microwaves both in the tunneling processes and in the spin dynamics. To test our theory we also present here experimental ESR-STM spectra measured in TiH molecules on a MgO substrate, a known spin-1/2 system, as a function of the external magnetic field and the bias voltage, see Fig. 1(c). Our theory is able to quantitatively reproduce all the salient features of the experimental results across many orders of magnitude in current, see Fig. 1(d) and discussion below. This quantitative agreement allows us in turn to unambiguously determine the relaxation and decoherence times of the system. Moreover, we supplement our theory with electromagnetic simulations to determine the magnitude of the electric and magnetic field in the region of the tunnel junction and to provide further insight as to what drives the ESR transitions in our experiments. Our study leads to a number of important conclusions for the field of ESR-STM, among which are the following ones:

(1) The transitions in our ESR-STM experiments are driven by the ac magnetic field that accompanies the microwave radiation.

(2) We confirm that the measured ESR signal is predominantly due to the change in magnetoresistance resulting from microwave-induced transitions. We provide an analytical formula for the ESR spectra that corroborates the

phenomenological expressions often employed in the literature. Our formula includes voltage and current dependence of the relaxation and decoherence times. It also reveals the need for a high spin polarization of the tips to obtain sizable ESR signals.

(3) A misalignment of the spins between the magnetic impurity and the STM tip results in a coupling of the magnetization dynamics to the microwave field, known as homodyne detection, which gives rise to an asymmetry in the ESR spectra often observed in this spectroscopy. This mechanism also explains our experimental ESR signal near zero bias voltage.

The rest of this manuscript is organized as follows. In Sec. II, we present our theory to describe the ESR-STM spectra in an arbitrary spin system. Then, in Sec. III, we apply this theory to the case of a spin-1/2 system. Section IV is devoted to a brief description of our experimental ESR-STM results obtained in TiH molecules on a MgO substrate and used to test our theory. We present in Sec. V an analysis of these experimental results in light of our theory and explain how the different rates and timescales can be extracted from such an analysis. In Sec. VI, we present electromagnetic simulations that aim at determining the magnitude of the electromagnetic fields at the junction region with the goal to clarify what determines the transitions in our ESR-STM experiments. Finally, we summarize the main conclusions of this work in Sec. VII. We also include two appendices to provide more details about our experiment, as well as to report some analytical results for the spin-1/2 system.

II. GENERAL ESR-STM THEORY

In this section, we present our general ESR-STM theory, which we will apply to a spin-1/2 system in the next section. The goal of this ESR-STM theory is to describe the electrical current through a spin system (or magnetic impurity) deposited on a substrate and addressed by an STM tip in the presence of a microwave field, see Fig. 1(a). Our approach is based on the use of a tunneling Hamiltonian that describes both the spin-flip processes that can occur in this system and the microwave-assisted processes induced by the microwave field. We use this tunneling Hamiltonian in combination with linear response theory to express the current in terms of spin correlation functions of the spin system. Those correlation functions are determined with the help of quantum master equations that describe the dynamics of the spin system. In the following, we explain how these different ingredients are combined to provide an ESR-STM theory for an arbitrary spin system.

A. Tunneling Hamiltonian

We model the tunnel junction depicted in Fig. 1(a) by a left and a right reservoir $H_{L,R}$, which correspond to the substrate and the STM tip, along with a tunnel coupling H_T , such that the total Hamiltonian becomes

$$H = H_L + H_R + H_T. \quad (1)$$

We do not specify the left and right reservoirs any further other than by the corresponding spin-dependent quasiparticle creation and annihilation operators $c_{L,R\sigma}^\dagger$ and $c_{L,R\sigma}$, respectively,

where σ denotes the spin index \uparrow or \downarrow for spin-1/2 particles. We describe the effective tunnel coupling between the two electrodes as follows

$$H_T(\tau) = t e^{i\phi(\tau)} \sum_{\sigma,\sigma'} c_{L\sigma}^\dagger(\tau) \left(\delta_{\sigma\sigma'} + \frac{\lambda}{\hbar} \boldsymbol{\sigma}_{\sigma\sigma'} \cdot \mathbf{S}(\tau) \right) c_{R\sigma'}(\tau) + \text{H.c.} \quad (2)$$

Here, τ denotes the time, t is a hopping matrix element, λ is a dimensionless constant, $\boldsymbol{\sigma} = (\sigma^x, \sigma^y, \sigma^z)$ is a vector formed by the three Pauli matrices, and $\mathbf{S}(\tau) = (S^x(\tau), S^y(\tau), S^z(\tau))$ denotes the spin of the magnetic impurity (for simplicity we consider here a single spin, but the theory can be readily generalized to the case of an arbitrary number of spins). The time-dependent phase accompanying the hopping is given by $\phi(\tau) = \omega_0 \tau + \alpha \sin(\omega_r \tau)$, where $\omega_0 = eV/\hbar$ (V being the dc bias voltage), ω_r is the microwave frequency, and $\alpha = eV_{ac}/\hbar\omega_r$ (V_{ac} being the ac bias voltage generated across the junction by the microwave field).

This tunneling Hamiltonian incorporates the two basic ingredients in ESR-STM: the elastic and inelastic electron tunneling, and the microwave field. The elastic and inelastic electron tunneling is accounted for by the term in the brackets in Eq. (2). The δ function describes the regular elastic tunneling, while the second term accounts for the interaction with the spin system during which the tunneling electrons may lose/gain energy. The dimensionless constant λ quantifies the relative contribution of this inelastic channel. In the absence of microwaves, Eq. (2) is the starting point of the established theory of single-spin inelastic tunneling spectroscopy [35–37], which has been confirmed in numerous experiments [32,37,38]. On the other hand, we also describe the effect of the microwave field in terms of an ac bias voltage V_{ac} in the junction. Here, we have used a standard unitary transformation to include the ac bias as a phase factor in the hopping matrix element [39,40]. The parameter α describes the strength of the coupling to the electromagnetic field. This approach follows the well-established theory of photon-assisted tunneling [41], which has extremely successfully explained the physics of microwave-irradiated experiments in atomic-scale systems [40,42–46]. We note that the approach that we are about to describe naturally reduces to the theory of single-spin inelastic tunneling spectroscopy in the absence of microwaves and to the photon-assisted tunneling theory in the absence of spin-flip tunneling.

For later convenience, we rewrite the tunneling Hamiltonian of Eq. (2) by separating the degrees of freedom related to the electrodes and to the spin system as follows

$$H_T(\tau) = t e^{i\phi(\tau)} \sum_{\mu} \sum_{\sigma,\sigma'} [c_{L\sigma}^\dagger(\tau) c_{R\sigma'}(\tau) + c_{R\sigma}^\dagger(\tau) c_{L\sigma'}(\tau)] \times \Lambda_{\sigma\sigma'}^\mu \otimes S^\mu(\tau), \quad (3)$$

where the index μ goes from 0 to 3, and we have defined

$$\Lambda_{\sigma\sigma'} = \left(\delta_{\sigma\sigma'}, \frac{\lambda}{2} \sigma_{\sigma\sigma'}^+, \frac{\lambda}{2} \sigma_{\sigma\sigma'}^-, \lambda \sigma_{\sigma\sigma'}^z \right), \quad (4)$$

$$\mathbf{S}(\tau) = \left(\mathbb{1}, \frac{1}{\hbar} S^-(\tau), \frac{1}{\hbar} S^+(\tau), \frac{1}{\hbar} S^z(\tau) \right), \quad (5)$$

where $\sigma_{\sigma\sigma'}^\pm = \sigma_{\sigma\sigma'}^x \pm i\sigma_{\sigma\sigma'}^y$, and $S^\pm = S^x \pm iS^y$.

B. Tunneling current

Within our model, the current operator is given by [40]

$$\hat{I}(\tau) = \frac{ie}{\hbar} \sum_{\sigma} [c_{L\sigma}^{\dagger}(\tau)c_{L\sigma}(\tau), H_{\Gamma}(\tau)]. \quad (6)$$

Using linear response theory [47] (i.e., first-order perturbation theory in H_{Γ}), the expectation value of the time-dependent

$$I(\tau) = \frac{2e}{\hbar} \sum_{n,m=-\infty}^{\infty} J_n(\alpha)J_{n+m}(\alpha) \sum_{\alpha,\beta} \int_{-\infty}^{\infty} d\omega \int_{-\infty}^{\infty} d\omega' \int_0^{\infty} \frac{d\tau'}{\hbar} \text{Re}\{[e^{in\omega_r\tau} e^{i(\omega-\omega')\tau'} \bar{\Gamma}_{\alpha\beta}(\omega, \omega' + \omega_0 + m\omega_r) - e^{-in\omega_r\tau} e^{-i(\omega-\omega')\tau'} \bar{\Gamma}_{\alpha\beta}(\omega, \omega' + \omega_0 + m\omega_r)] \langle \mathcal{S}^{\alpha\dagger}(\tau)\mathcal{S}^{\beta}(\tau - \tau') \rangle_0\}, \quad (8)$$

Here, $J_n(\alpha)$ is a Bessel function of the first kind of order n and $\langle A \rangle_0 = \text{Tr}[\rho(\tau)A]$, with $\rho(\tau)$ being the reduced density operator of the spin system which will be determined below. Moreover, we have introduced the spectral rates

$$\bar{\Gamma}_{\alpha\beta}(\omega, \omega') = t^2 \text{Tr}[g_L^{+-}(\omega)\Lambda^{\alpha\dagger}g_R^{-+}(\omega')\Lambda^{\beta}], \quad (9)$$

$$\bar{\Gamma}_{\alpha\beta}(\omega, \omega') = t^2 \text{Tr}[g_L^{-+}(\omega)\Lambda^{\beta}g_R^{+-}(\omega')\Lambda^{\alpha\dagger}], \quad (10)$$

associated with electron transitions from the left electrode to the right one and vice versa. The same spectral rates will also later be used to calculate the dissipator [cf. Eq. (15)] in the equation of motion for the density matrix $\rho(\tau)$. These functions are expressed in terms of the lead Green's functions defined as

$$g_{j\sigma\sigma'}^{+-}(\omega) = i \int_{-\infty}^{\infty} e^{i\omega\tau} \langle c_{j\sigma'}^{\dagger}(0)c_{j\sigma}(\tau) \rangle_0 d\tau, \quad (11)$$

$$g_{j\sigma\sigma'}^{-+}(\omega) = -i \int_{-\infty}^{\infty} e^{i\omega\tau} \langle c_{j\sigma}(\tau)c_{j\sigma'}^{\dagger}(0) \rangle_0 d\tau. \quad (12)$$

where $j = L, R$. The Green's functions describe the electronic structure of the electrodes and also contain the information of the occupation factors. Finally, the trace Tr appearing in Eqs. (9) and (10) refers to the 2×2 spin space. Thus the current is expressed in terms of the basic properties of the electrodes via their Green's functions, and spin correlation functions of the magnetic system. The Green's functions will be specified in more detail below when we discuss the comparison with the experiments. The calculation of the correlation functions of the spin system will be detailed in the next subsection.

C. Dynamics of a general spin system

To complete the calculation of the current we need to compute the spin correlation functions $\langle \mathcal{S}^{\alpha\dagger}(\tau)\mathcal{S}^{\beta}(\tau - \tau') \rangle_0$ entering Eq. (8). To do so, we determine the reduced density matrix of the spin system $\rho(\tau)$ by employing standard techniques of the theory of open quantum systems. There are different approaches to obtain the quantum master equation describing the dynamics of the reduced density matrix, such as the Bloch-Redfield equations [48]. We find it more convenient to use the Lindblad approach and we shall follow

current can be expressed as

$$I(\tau) = -\frac{i}{\hbar} \int_{-\infty}^{\tau} \langle [\hat{I}(\tau), H_{\Gamma}(\tau')] \rangle_0 d\tau', \quad (7)$$

where $\langle \cdot \rangle_0$ denotes an expectation value computed in the absence of the perturbation given by H_{Γ} . Making now use of Eq. (3) and Wick's theorem [47], it can be shown that the time-dependent current in the presence of microwaves is given by

closely Ref. [49]. Within the Lindblad approach, $\rho(\tau)$ satisfies the following equation of motion in the interaction picture [49]

$$\frac{d\rho(\tau)}{d\tau} = -\frac{i}{\hbar} [H_r(\tau) + H_{\text{LS}}, \rho(\tau)] + \mathcal{D}[\rho(\tau)], \quad (13)$$

where $H_r(\tau)$ describes the interaction with the microwave (specified in more detail below), H_{LS} is the Lamb shift Hamiltonian, and $\mathcal{D}[\rho(\tau)]$ is the dissipator operator. The expressions for H_{LS} and $\mathcal{D}[\rho(\tau)]$ depend on the system-bath interaction H_I . To proceed, we shall assume that H_I can be factorized as follows

$$H_I = \sum_{\alpha} A_{\alpha} \otimes B_{\alpha}, \quad (14)$$

where A is an operator related to the spin system and B is a bath operator. With this decomposition, the dissipator and the Lamb shift Hamiltonian are given by [49]

$$\mathcal{D}[\rho(\tau)] = \frac{1}{\hbar^2} \sum_{\omega} \sum_{\alpha\beta} \gamma_{\alpha\beta}(\omega) [A_{\beta}(\omega)\rho(\tau)A_{\alpha}^{\dagger}(\omega) - \frac{1}{2} \{A_{\alpha}^{\dagger}(\omega)A_{\beta}(\omega), \rho(\tau)\}], \quad (15)$$

$$\mathcal{H}_{\text{LS}} = \frac{1}{\hbar} \sum_{\omega} \sum_{\alpha\beta} h_{\alpha\beta}(\omega) A_{\alpha}^{\dagger}(\omega) A_{\beta}(\omega), \quad (16)$$

where

$$\frac{1}{2} \gamma_{\alpha\beta}(\omega) + ih_{\alpha\beta}(\omega) = \int_0^{\infty} d\tau e^{i\omega\tau} \langle B_{\alpha}^{\dagger}(\tau)B_{\beta}(0) \rangle. \quad (17)$$

In Eqs. (15) and (16), we have defined the operator

$$A_{\alpha}(\omega) = \sum_{\varepsilon' - \varepsilon = \omega} \mathcal{P}(\varepsilon') A_{\alpha} \mathcal{P}(\varepsilon). \quad (18)$$

Here, $\mathcal{P}(\varepsilon)$ is a projection operator onto the eigenstate of H_S belonging to the eigenvalue ε and the sum is over all pairs of states with energy ε and ε' having the energy difference $\omega = \varepsilon' - \varepsilon$.

There are three natural baths that can contribute to the relaxation and decoherence of the spin system: the tunneling electrons, the microwave field, and the substrate. For simplicity, we shall assume that the action of these different

baths is additive (i.e., they are independent). We include the impact of the tunneling electrons on the spin dynamics using the general formalism above. In this case, the system-bath interaction H_I is given by H_T in Eq. (3) without microwaves (i.e., $\alpha = 0$). Thus we find that $A_\alpha = \mathcal{S}^\alpha$, see Eq. (5), and $B_\alpha(\tau) = t \sum_{\sigma, \sigma'} [c_{L\sigma}^\dagger(\tau) c_{R\sigma'}(\tau) + c_{R\sigma}^\dagger(\tau) c_{L\sigma'}(\tau)] \Lambda_{\sigma\sigma'}^\alpha$, where the index α runs from 0 to 3 [cf. Eq. (4)]. The quantities $\gamma_{\alpha\beta}(\omega)$ and $h_{\alpha\beta}(\omega)$ can be expressed in terms of the spectral rates of Eqs. (9) and (10) as follows:

$$\gamma_{\alpha\beta}(\omega) = \int_{-\infty}^{\infty} \frac{d\omega_1}{2\pi} \{ \bar{\Gamma}_{\alpha\beta}(\omega_1, \omega_1 + \omega_0 + \omega) + \bar{\Gamma}_{\alpha\beta}(\omega_1, \omega_1 + \omega_0 - \omega) \}, \quad (19)$$

$$h_{\alpha\beta}(\omega) = \int_{-\infty}^{\infty} \frac{d\omega_1}{2\pi} \int_{-\infty}^{\infty} \frac{d\omega_2}{2\pi} \left\{ \frac{\bar{\Gamma}_{\alpha\beta}(\omega_1, \omega_2)}{\omega + \omega_2 - \omega_1 - \omega_0} + \frac{\bar{\Gamma}_{\alpha\beta}(\omega_1, \omega_2)}{\omega - \omega_2 + \omega_1 + \omega_0} \right\}. \quad (20)$$

The interaction between the spin system and the substrate can be treated essentially in the same way as the tunneling electrons, while the impact of the microwave field (in the form of spontaneous emission) is a textbook result that we shall simply borrow here [48]. We shall be more specific on how we model these two interactions in our discussion of a spin-1/2 system in Sec. III A.

III. APPLICATION TO A SPIN-1/2 SYSTEM

Let us now apply the general theory described in Sec. II to the case of a spin-1/2 system. Upon application of a static magnetic field, the two degenerate spin levels are Zeeman-split and this two-level system can be described by the Hamiltonian: $H_S = \hbar\omega_a |a\rangle \langle a| + \hbar\omega_b |b\rangle \langle b|$ where state $|a\rangle$ is

the spin-up state (or ground state) and $|b\rangle$ is the spin-down state (or excited state). This Hamiltonian can be written in a standard matrix form as $H_S = \frac{1}{2}\hbar\omega_{ba}\sigma^z$, where $\omega_{ba} = \omega_b - \omega_a > 0$. The interaction with the radiation field is given by

$$H_r(\tau) = -\hbar\Omega \cos(\omega_r\tau)\sigma^x, \quad (21)$$

where Ω is the Rabi frequency carrying the information of the intensity of the microwave drive. At this point, we do not need to further specify the origin of the Rabi frequency. However, it must be related to the ac magnetic field in the junction region, as we discuss in Sec. VI. In the following, we shall discuss the results of the general theory applied to this two-level system.

A. Spin dynamics

The density matrix of a spin-1/2 system is a 2×2 matrix. For a pure system, it is defined as $\rho = |\psi\rangle \langle \psi|$, where $|\psi\rangle$ is the wave function of the two-level system in the basis $\{|a\rangle, |b\rangle\}$. For this system, the dissipator and the Lamb shift operators adopt the form

$$\mathcal{D}[\rho] = \Gamma_{a \rightarrow b} \begin{pmatrix} -\rho_{aa} & \rho_{ab}/2 \\ \rho_{ba}/2 & \rho_{bb} \end{pmatrix} + \Gamma_{b \rightarrow a} \begin{pmatrix} \rho_{aa} & \rho_{ab}/2 \\ \rho_{ba} & -\rho_{bb} \end{pmatrix} - \Gamma_{ab}^{\text{ad}} \begin{pmatrix} 0 & \rho_{ab} \\ \rho_{ba} & 0 \end{pmatrix}, \quad (22)$$

$$\mathcal{H}_{\text{LS}} = \frac{\hbar\Delta_{ab}}{2} \begin{pmatrix} 1 & 0 \\ 0 & -1 \end{pmatrix}. \quad (23)$$

Here, $\Gamma_{a \rightarrow b} \equiv \gamma_{11}(-\omega_{ba})/\hbar^2$ is the transition rate from a to b , $\Gamma_{b \rightarrow a} \equiv \gamma_{22}(\omega_{ba})/\hbar^2 + \Gamma_0$ is the transition rate from b to a , $\Gamma_{ab}^{\text{ad}} \equiv \gamma_{33}(0)/2\hbar^2 + \gamma_0$ is the pure decoherence rate. The renormalization energy $\Delta_{ab} = \Delta_{ab}^{\text{ad}} + \Delta_{ab}^{\text{nonad}}$ consists of two contributions: an adiabatic energy renormalization $\Delta_{ab}^{\text{ad}} = h_{03}(0)/\hbar^2$ and a nonadiabatic energy renormalization $\Delta_{ab}^{\text{nonad}} = [h_{11}(-\omega_{ba}) - h_{22}(\omega_{ba})]/\hbar^2$. Explicit expressions for these parameters follow from Eqs. (19)-(20) and are given by

$$\Gamma_{a \rightarrow b} = \left(\frac{\lambda t}{\hbar} \right)^2 \int_{-\infty}^{\infty} \frac{d\omega}{2\pi} [g_{L\downarrow}^{+-}(\omega)g_{R\uparrow}^{-+}(\omega + \omega_0 - \omega_{ba}) + g_{L\uparrow}^{+-}(\omega)g_{R\downarrow}^{+-}(\omega + \omega_0 + \omega_{ba})], \quad (24)$$

$$\Gamma_{b \rightarrow a} = \left(\frac{\lambda t}{\hbar} \right)^2 \int_{-\infty}^{\infty} \frac{d\omega}{2\pi} [g_{L\uparrow}^{+-}(\omega)g_{R\downarrow}^{-+}(\omega + \omega_0 + \omega_{ba}) + g_{L\downarrow}^{+-}(\omega)g_{R\uparrow}^{-+}(\omega + \omega_0 - \omega_{ba})] + \Gamma_0, \quad (25)$$

$$\Gamma_{ab}^{\text{ad}} = \frac{1}{2} \left(\frac{\lambda t}{\hbar} \right)^2 \int_{-\infty}^{\infty} \frac{d\omega}{2\pi} [g_{L\uparrow}^{+-}(\omega)g_{R\uparrow}^{-+}(\omega + \omega_0) + g_{L\uparrow}^{-+}(\omega)g_{R\uparrow}^{+-}(\omega + \omega_0) + g_{L\downarrow}^{+-}(\omega)g_{R\downarrow}^{-+}(\omega + \omega_0) + g_{L\downarrow}^{-+}(\omega)g_{R\downarrow}^{+-}(\omega + \omega_0)] + \gamma_0, \quad (26)$$

$$\Delta_{ab}^{\text{ad}} = \frac{2\lambda^2}{\hbar^2} \int_{-\infty}^{\infty} \frac{d\omega}{2\pi} \int_{-\infty}^{\infty} \frac{d\omega'}{2\pi} \frac{g_{L\uparrow}^{+-}(\omega)g_{R\uparrow}^{+-}(\omega') + g_{L\downarrow}^{+-}(\omega)g_{R\downarrow}^{+-}(\omega') - g_{L\downarrow}^{-+}(\omega)g_{R\downarrow}^{-+}(\omega') - g_{L\uparrow}^{-+}(\omega)g_{R\uparrow}^{-+}(\omega')}{\omega' - \omega - \omega_0}, \quad (27)$$

$$\Delta_{ab}^{\text{nonad}} = \left(\frac{\lambda t}{\hbar} \right)^2 \int_{-\infty}^{\infty} \frac{d\omega}{2\pi} \int_{-\infty}^{\infty} \frac{d\omega'}{2\pi} \left\{ \frac{g_{L\uparrow}^{+-}(\omega)g_{R\downarrow}^{-+}(\omega') + g_{L\uparrow}^{-+}(\omega)g_{R\downarrow}^{-+}(\omega')}{\omega' - \omega - \omega_0 - \omega_{ba}} - \frac{g_{L\downarrow}^{-+}(\omega)g_{R\uparrow}^{-+}(\omega') + g_{L\downarrow}^{+-}(\omega)g_{R\uparrow}^{-+}(\omega')}{\omega' - \omega - \omega_0 + \omega_{ba}} \right\}. \quad (28)$$

The parameters Γ_0 and γ_0 are introduced here as phenomenological decay and decoherence rates, respectively, that carry contributions from both the substrate coupling and spontaneous emission. We have assumed that the lead Green's functions are diagonal in spin space (i.e., no spin mixing in the electrodes). Also, the Lamb shift may be absorbed

in the bare frequency ω_{ab} , as it is usually done in different contexts [50]. However, the Lamb shift may be non-negligible affecting the determination of the value for the tip magnetic field. In addition, the previous expressions are analyzed in Appendix B in relevant limiting cases to give analytical insight.

In a rotating frame (rotating with the same frequency as the microwave enabling us to use the rotating-wave approximation where $\omega_{ba} \sim \omega_r$), the quantum master equation for the density matrix in terms of the quantities defined above adopts the form

$$\frac{d\rho_{aa}(\tau)}{d\tau} = -\frac{i\Omega}{2}[\tilde{\rho}_{ba}(\tau) - \tilde{\rho}_{ab}(\tau)] - \Gamma_{a \rightarrow b}\rho_{aa}(\tau) + \Gamma_{b \rightarrow a}\rho_{bb}(\tau), \quad (29)$$

$$\frac{d\rho_{bb}(\tau)}{d\tau} = \frac{i\Omega}{2}[\tilde{\rho}_{ba}(\tau) - \tilde{\rho}_{ab}(\tau)] - \Gamma_{b \rightarrow a}\rho_{bb}(\tau) + \Gamma_{a \rightarrow b}\rho_{aa}(\tau), \quad (30)$$

$$\frac{d\tilde{\rho}_{ab}(\tau)}{d\tau} = -\frac{i\Omega}{2}[\rho_{bb}(\tau) - \rho_{aa}(\tau)] - (\gamma + i\delta)\tilde{\rho}_{ab}(\tau). \quad (31)$$

$$\tilde{\rho}(\tau \rightarrow \infty) = \frac{1}{2(\delta^2 + \gamma^2)\Gamma + 2\gamma\Omega^2} \begin{pmatrix} \gamma\Omega^2 + 2\Gamma_{b \rightarrow a}(\delta^2 + \gamma^2) & \Omega\Gamma'(\delta + i\gamma) \\ \Omega\Gamma'(\delta - i\gamma) & \gamma\Omega^2 + 2\Gamma_{a \rightarrow b}(\delta^2 + \gamma^2) \end{pmatrix}, \quad (33)$$

where $\rho_{aa,bb}(\tau) = \tilde{\rho}_{aa,bb}$, $\rho_{ab}(\tau) = e^{i(\omega_r - \omega_{ba})\tau} \tilde{\rho}_{ab}$. We also used the abbreviation

$$\Gamma = \Gamma_{b \rightarrow a} + \Gamma_{a \rightarrow b} \quad \text{and} \quad \Gamma' = \Gamma_{b \rightarrow a} - \Gamma_{a \rightarrow b}. \quad (34)$$

The solution for the density matrix in Eq. (33) can be used in Eq. (8) for the calculation of the dc current, which will be done in the next subsection.

With knowledge of the decay and decoherence rates we can determine the characteristic timescales for relaxation and decoherence of the spin system. Following Refs. [28,38], we define the following timescales:

$$T_1 = \frac{1}{\Gamma}, \quad T_2^* = \frac{1}{\Gamma_{ab}^{\text{ad}}}, \quad T_2 = \frac{1}{\gamma}, \quad (35)$$

where T_1 represents the relaxation time, T_2^* the pure decoherence time, and T_2 the total decoherence time. We note that all of these times depend on the applied bias voltage and correspondingly on the tunneling current through Eqs. (24) to (26).

B. DC current

We are now in position to provide the key results for the current in a spin-1/2 system. We shall focus on the dc current and consider first the special case, in which the spin of the magnetic impurity is parallel to the spin quantization axis in the STM tip (due to a high static magnetic field that aligns all spins in the system). In this case, the dc current adopts a very appealing form given by

$$I(V, \alpha) = \sum_{n=-\infty}^{\infty} J_n^2(\alpha) I^{\text{dark}}(V + n\hbar\omega_r/e), \quad (36)$$

where $I^{\text{dark}}(V)$ is formally the current in absence of microwaves, but all the properties of the spin system have to be computed taking into account the effect of the microwave field. Notice that Eq. (36) has the form of the Tien-Gordon formula that is well-known in the context of photon-assisted

Here, $\tilde{\rho}_{ba} = \tilde{\rho}_{ab}^*$, $\rho_{ab}(\tau) = e^{i(\omega_r - \omega_{ba})\tau} \tilde{\rho}_{ab}$ is the relation between the rotating frame and the interaction picture density matrix. Furthermore, γ is the effective decoherence rate defined as

$$\gamma = \Gamma_{ab}^{\text{ad}} + (\Gamma_{b \rightarrow a} + \Gamma_{a \rightarrow b})/2, \quad (32)$$

and $\delta = \omega_r - \omega_{ba} + \Delta_{ab}$ is the detuning of the microwaves (including the second order perturbation to the energy gap Δ_{ab}).

In this work, we focus on the case of continuous illumination, where in the long time limit, we reach a stationary situation for ρ_{aa} , ρ_{bb} and $\tilde{\rho}_{ab}$. The stationary solution for this rotating frame is given by

tunneling [40–42]. The dark current is given by the sum of three contributions

$$I^{\text{dark}}(V) = I_{\text{el}}(V) + I_{\text{int}}(V) + I_{\text{inel}}(V), \quad (37)$$

which are given in terms of the electrode Green's functions and the elements of the stationary density matrix of Eq. (33) as follows:

$$I_{\text{el}}(V) = \frac{4\pi^2 e t^2}{h} \sum_{\sigma} \int_{-\infty}^{\infty} \varrho_{L\sigma}(E - eV) \varrho_{R\sigma}(E) \times [f(E - eV) - f(E)] dE = I_{\text{el}}^{\uparrow}(V) + I_{\text{el}}^{\downarrow}(V), \quad (38)$$

$$I_{\text{int}}(V) = \frac{2\lambda}{\hbar} \langle S^z \rangle [I_{\text{el}}^{\uparrow}(V) - I_{\text{el}}^{\downarrow}(V)] = \lambda [I_{\text{el}}^{\uparrow}(V) - I_{\text{el}}^{\downarrow}(V)] \times (\rho_{aa} - \rho_{bb}), \quad (39)$$

$$I_{\text{inel}}(V) = \frac{\lambda^2}{4} I_{\text{el}}(V) - \frac{\lambda^2}{2} [I_+(V) + I_-(V)] + \frac{\lambda^2}{2} [I_+(V) - I_-(V)] (\rho_{aa} - \rho_{bb}), \quad (40)$$

with the definitions

$$I_+(V) = \frac{et^2}{h} \int_{-\infty}^{\infty} [g_{L\downarrow}^{+-}(E) g_{R\uparrow}^{-+}(E + eV - \hbar\omega_{ba}) - g_{L\uparrow}^{-+}(E) g_{R\downarrow}^{+-}(E + eV + \hbar\omega_{ba})] dE, \\ I_-(V) = \frac{et^2}{h} \int_{-\infty}^{\infty} [g_{L\uparrow}^{+-}(E) g_{R\downarrow}^{-+}(E + eV + \hbar\omega_{ba}) - g_{L\downarrow}^{-+}(E) g_{R\uparrow}^{+-}(E + eV - \hbar\omega_{ba})] dE.$$

Here, $\varrho_{j\sigma}(E)$ is the density of states (DOS) of electrode $j = L, R$ and $f(E)$ is the Fermi function. The first contribution $I_{\text{el}}(V)$ is the elastic current flowing through the

junction, which is given by the standard tunneling formula. The third contribution $I_{\text{inel}}(V)$ is the inelastic current that results from the spin-flip processes undergone by the tunneling electrons. The second contribution $I_{\text{int}}(V)$, which we refer to as interference current, can be seen as resulting from the interference between the two previous processes. The second term is expected to dominate the signal involving the spin system because it is first order in λ (this is confirmed below by our comparison with the experiments). This interference term is proportional to both the spin polarization of the spin system along the z direction $\langle S^z \rangle = \frac{\hbar}{2}(\rho_{aa} - \rho_{bb})$ and to the current polarization $I_{\text{pol}}(V) \equiv I_{\text{el}}^{\uparrow}(V) - I_{\text{el}}^{\downarrow}(V)$ in the absence of microwaves. Therefore this contribution is only finite when there is a population difference ($\rho_{aa} \neq \rho_{bb}$) and moreover the elastic current has a finite spin polarization. This explains the need for a spin-polarized tip to observe an ESR signal and shows that *ESR spectra are a measure of the change in magnetoresistance that results from the resonant transitions between the electronic levels induced by the microwave field*. It is also worth mentioning that the inelastic term of Eq. (40) also contributes to the ESR signal, which requires a finite current polarization as well. The contribution of the interference and inelastic terms to the ESR spectrum can be computed combining Eqs. (39) and (40) with Eq. (36). Defining the ESR lineshape by subtracting the off-resonant current (for $\delta \rightarrow \infty$), we arrive at the following expression describing the ESR signal in terms of the relaxation and decoherence times [cf. Eq. (35)]

$$\text{ESR}(\delta) = I_{\text{sat}} \left(\frac{\Omega^2 T_1 T_2}{\delta^2 T_2^2 + 1 + \Omega^2 T_1 T_2} \right), \quad (41)$$

where we have defined

$$I_{\text{sat}} = -\lambda \sum_n J_n^2(\alpha) I_{\text{pol}}(V + n\hbar\omega_r/e) - \frac{\lambda^2}{2} \sum_n J_n^2(\alpha) \times [L_+(V + n\hbar\omega_r/e) - L_-(V + n\hbar\omega_r/e)]. \quad (42)$$

Equation (41) predicts an ESR peak height given by

$$I_{\text{peak}} = I_{\text{sat}} \frac{\Omega^2 T_1 T_2}{1 + \Omega^2 T_1 T_2}, \quad (43)$$

where I_{sat} is the saturation value of the current peak when $\Omega \rightarrow \infty$. The corresponding line width is given by $\mathcal{W} = \frac{1}{T_2} \sqrt{1 + \Omega^2 T_1 T_2}$. These results coincide with the phenomenological formulas that have been employed to describe the experimental ESR spectra, see e.g., Refs. [3,6]. Thus our derivation here can be seen as a rigorous justification of those heuristic formulas. We point out here that the time scales T_1 and T_2 in these formulas are not phenomenological parameters, but they are given by the expressions of Eqs. (35) and (24)–(26) which make clear predictions about their dependence on the bias voltage and the tip-sample distance (encoded in the hopping parameter t). Moreover, Eq. (42) contains the information about the degree of spin polarization of a STM tip to obtain sizable ESR signals. In Appendix B, we provide additional analytical insight into these results.

The current in the absence of microwaves can be obtained by setting $\alpha = 0$ in the equations above. In that case, the current is given by the dark current in Eqs. (37)–(40), where

the density matrix elements ρ_{aa} and ρ_{bb} are computed in the absence of microwaves. Furthermore, the result for the current coincides with the results reported in the literature in the absence of microwaves [35–37]. Lastly, the division into three current contributions above is not generic of a spin-1/2 system, but applies to any spin system.

C. Homodyne detection

In the previous section, we have assumed that the spins of the system and the tip polarization are parallel. This led us to a result for the ESR line shape summarized in Eq. (41) that predicts symmetric spectra with respect to the detuning δ . However, asymmetric spectra have been reported in the literature [6,8,12], in particular close to zero bias voltage, which we will discuss below. In the following, we assume that the asymmetry arises when the static magnetic field does not completely align the tip and impurity spin. Other proposals trace the origin of the asymmetry back to the failure of the rotating wave approximation [51]. Focusing on the two-level system, if the impurity spin and the magnetization of the tip are not collinear and form an angle $\theta \neq 0$, one can show that this induces a Larmor precession of the impurity magnetization, i.e., when $\omega_r \approx \omega_{ba}$, this leads to an expectation value for $S^z(\tau)$ of the form

$$\langle S^z(\tau) \rangle = \frac{\hbar \cos \theta}{2} [\rho_{aa}(\delta) - \rho_{bb}(\delta)] + \frac{\hbar \sin \theta}{2} [\tilde{\rho}_{ba}(\delta) e^{-i\omega_r \tau} + \tilde{\rho}_{ab}(\delta) e^{i\omega_r \tau}]. \quad (44)$$

The second term here is time-dependent, which is determined by the coherences (i.e., off-diagonal elements) in the reduced density matrix. This time-dependent magnetization couples to the microwave field to give an additional contribution to the dc current. This effect has been referred to as *homodyne detection* [6], in analogy to what has been observed in the context of electric-field induced ferromagnetic resonance excitation [52]. The dc current in this case can be obtained by inserting Eq. (44) into Eq. (8). The main effect of the homodyne detection is the modification of the interference term, whose contribution to the dc current in the presence of microwaves becomes

$$I_{\text{int}}(V, \alpha) = \lambda \sum_{n=-\infty}^{\infty} J_n^2(\alpha) I_{\text{pol}}(V + n\hbar\omega_r/e) \times \left[(\rho_{aa} - \rho_{bb}) \cos \theta + \frac{2n}{\alpha} \text{Re}\{\tilde{\rho}_{ba}\} \sin \theta \right]. \quad (45)$$

The first term inside the brackets gives the contribution that we have discussed in Sec. III B, but it is rescaled by $\cos \theta$. The second term is proportional to $\sin \theta$ and describes the new contribution that depends on the real part of the coherence, which is odd in δ . As we shall show below where we analyze our own experimental results, this term is responsible for the asymmetry in the ESR spectra and explains the unconventional spectral line shapes near zero bias voltage.

IV. EXPERIMENTAL RESULTS

With the theory described in previous sections, we can now not only quantitatively analyze the measured ESR signal, but also understand this signal in relation to the background signal. We can also describe the tunneling current with and without microwaves, which carries important information that allows us to independently determine the model parameters. Additionally, we can use this theory to analyze the ESR signal as a function of applied magnetic field and/or microwave frequency, and also as function of applied bias voltage, which provides a stringent test of the theory. In this section, we shall briefly discuss the experiments that were carried out to test the theory developed in this work.

As a testbed system for our theory we measured the ESR signal of a TiH molecule on MgO/Ag(100) as function of magnetic field and applied bias voltage, which is summarized in Fig. 1(c). The TiH molecule forms a spin-1/2 system on the MgO surface as has been observed in a number of different experiments before [7,13,16,21,53]. The microwave is fed through an antenna, which radiates towards the tunnel junction through vacuum [54]. The microwave amplitude and frequency were kept constant during the measurements, while the magnetic field was swept. The data were acquired by chopping the microwave (on/off) at a frequency of 107 Hz and detecting the signal in the tunneling current using a lock-in amplifier at that frequency [15,55,56]. The resulting measured current ΔI is effectively the difference between the tunneling current while the microwave is on I_{on} and the tunneling current while the microwave is off I_{off} ,

$$\Delta I = I_{\text{on}} - I_{\text{off}}. \quad (46)$$

Therefore we have to calculate the tunneling current with and without the microwave radiating into the tunnel junction. Due to the sinusoidal sampling of the lock-in amplifier, the measured ESR signal will be smaller by a factor of $\pi/2$ compared to the calculated difference of the tunneling current with the microwave on and off. This has to be taken into account for a quantitative analysis. We will do so implicitly in the following. Further details on the experimental setup and measurements can be found in Appendix A.

As one can see in Fig. 1(c), there is a clear ESR peak whose height and width evolves with the bias voltage in a nontrivial manner, which the theory must explain. Notice also that there is linear dependence of the ESR peak position on the the bias voltage. We attribute this dependence to spin-electric coupling in the tunnel junction [21], which we will only take into account phenomenologically here. On the other hand, the horizontal stripes are due to the tunneling electrons interacting with the microwave, which is not directly related to the ESR signal. In Fig. 1(d), the corresponding calculated spectra using the theory of Sec. III are shown for the same parameter range as in Fig. 1(c), which are in good quantitative agreement with the experimental data. The details of how we calculated the theoretical spectra will be described in detail in the following section.

TABLE I. Model parameters The parameters that are related to the tunneling current can be determined independently from a reference spectrum measured without microwaves (Ref.), the remaining parameters are determined from the ESR spectrum itself (Data). The temperature T and the microwave frequency ω_r are treated as input parameters (Input), which are given by the experimental setup. They are normalized such that the parameter τ_0 provides the corresponding channel transmission at the Fermi level. The microwave couples differently to the tunneling current and to the spin system. As the relation between these coupling mechanisms is still under debate, we use two parameters V_{ac} and $\hbar\Omega$ to describe the interaction with the microwave.

Symbol	Parameter	Fitted value	Source
p	tip polarization	-0.8	Ref.
τ_0	transmission	1.85×10^{-5}	Ref.
τ_1/τ_0	DOS linear coefficient	-2.7 eV^{-1}	Ref.
τ_2/τ_0	DOS quadratic coefficient	5 eV^{-2}	Ref.
λ	spin-flip parameter	0.46	Ref.
$\hbar\Gamma_0$	intrinsic decay rate	9 neV	Ref.
T	temperature	310 mK	Input
ω_r	microwave frequency	61 GHz	Input
$\omega_{\text{max}}, B_{\text{max}}$	ESR peak position	V dependent	Data
V_{ac}	microwave amplitude	19.9 mV	Data
$\hbar\Omega$	Rabi frequency	29 neV	Data
$\hbar\gamma_0$	intrinsic coherence rate	70 neV	Data
θ	homodyne angle	4.5°	Data

V. COMPARISON WITH THE EXPERIMENTAL RESULTS

In this section, we apply the results of the theory for a spin-1/2 system discussed in Sec. III to the analysis of our experimental results. This analysis proceeds in two steps. First, we fit the tunneling current in the absence of microwaves, which allows us to determine most of the parameters of the model, except those related to the microwave field. Then, we use those parameters to reproduce the ESR spectra of Fig. 1(c).

Despite the rather complex model involving a number of different interactions with the environment, the amount of parameters in the model remains manageable. A summary of the parameters, which we will use in the following, is given in Table I. The parameters that are relevant the tunneling current (marked ‘‘Ref.’’ in Table I) can be extracted from reference spectra without microwaves. The other parameters (marked ‘‘Data’’ in Table I) can be extracted from the ESR signal as well as the background signal. This provides enhanced consistency in determining the model parameters for a quantitative analysis of the ESR data.

We describe this procedure in more detail in the remainder of this section.

A. Current in the absence of microwaves

In Figs. 2(a) and 2(b), we show the experimental data for the current and differential conductance, respectively, as a function of the dc bias voltage in the absence of microwaves. Notice that the current is nonlinear. It exhibits a conductance step in the low bias voltage regime making it asymmetric with respect to the voltage polarity. To model these current-voltage

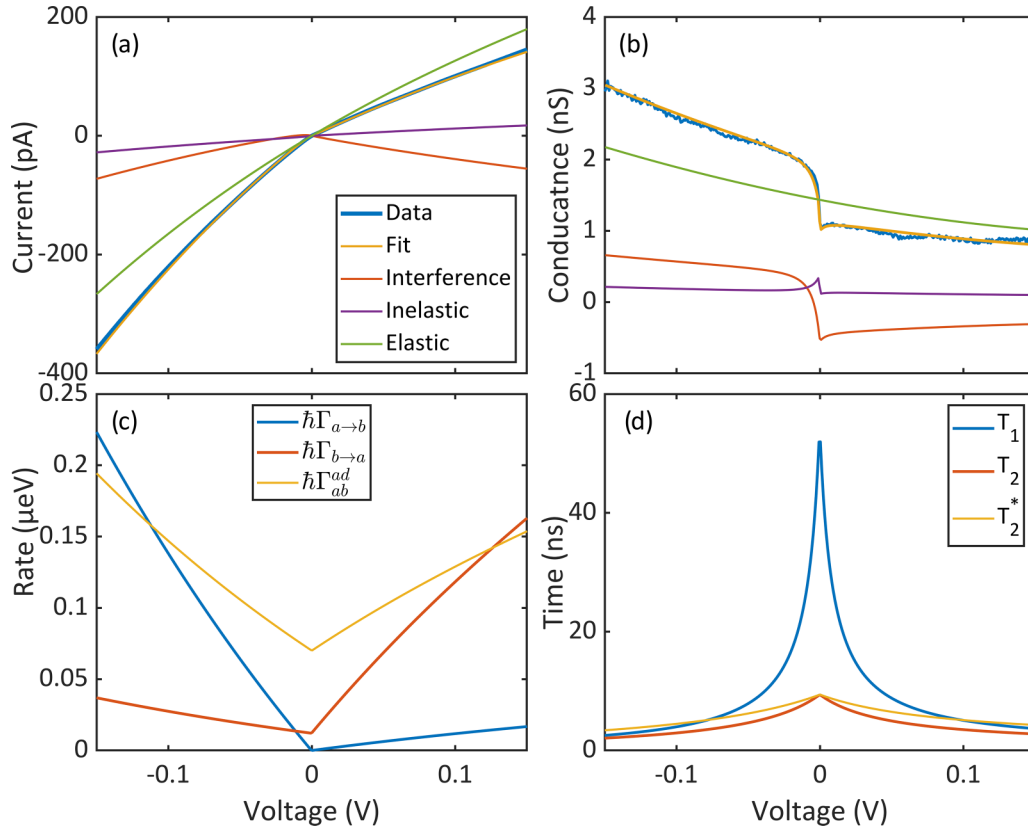


FIG. 2. Reference measurement without microwaves. (a) Current measurement and (b) simultaneous conductance measurement without microwaves as a reference to extract the tunneling parameters. The data is shown in blue and the fit is shown in red. The different contributions to the tunneling current are the elastic term (green), the interference term (yellow) and the inelastic term (purple). (c) Relaxation and decoherence rates for the data set in (a). (d) The corresponding relaxation and decoherence times as defined in Eq. (35).

characteristics we shall take into account two features of the lead Green's functions defined in Eqs. (11) and (12). The first feature is an energy-dependent DOS and the second feature is a spin-polarized DOS. Assuming that the lead Green's functions are diagonal in spin space, they are given by

$$g_{j\sigma}^{+-}(E) = 2\pi i \varrho_{j\sigma}(E) f(E), \quad (47)$$

$$g_{j\sigma}^{-+}(E) = 2\pi i \varrho_{j\sigma}(E) [f(E) - 1], \quad (48)$$

where $\varrho_{j\sigma}(E)$ is the DOS of electrode $j = L, R$ for spin $\sigma = \uparrow, \downarrow$ and $f(E) = [1 + \exp(E/k_B T)]^{-1}$ is the Fermi function. Then, to incorporate those two features, we assume that the substrate's DOS is constant and spin-independent ($\varrho_{L\sigma}(E) \approx \varrho_{L\sigma}(0)$, where the Fermi level is at $E = 0$), while the DOS of the right electrode (STM tip) is given by

$$\varrho_{R\sigma}(E) \approx (1 \pm p) \left[\varrho_R(0) + \varrho_R'(0)E + \frac{1}{2} \varrho_R''(0)E^2 \right]. \quad (49)$$

Here, $p \in [-1, 1]$ is the spin polarization of the tip, which is responsible for the current polarization I_{pol} being nonzero. The + sign applies to $\sigma = \uparrow$, while the - sign to $\sigma = \downarrow$. The different terms in the expansion of Eq. (49) can be cast into an energy dependent transmission coefficient $\tau(E) = \tau_0 + \tau_1 E + \tau_2 E^2$ with the coefficients $\tau_0 = 4\pi^2 t^2 \varrho_L(0) \varrho_R(0)$, $\tau_1 = 4\pi^2 t^2 \varrho_L(0) \varrho_R'(0)$ and $\tau_2 = 2\pi^2 t^2 \varrho_L(0) \varrho_R''(0)$. The transmission determines the magnitude of the elastic current, see Eq. (38). Note that τ_0 is just the transmission coefficient at

the Fermi level that determines the constant conductance. We also point out that the symmetry of the problem in principle allows us to exchange the densities of states in tip and sample without changing the result as long as the spin polarization is energy independent. Therefore, to lowest order, the actual energy dependence of the individual densities of states is not relevant, as long as the convolution matches the data.

Using these assumptions for the electronic structure of the electrodes, the temperature of the experiment ($T = 0.31$ K), and the current formula in the absence of microwaves described in Sec. III B in Eqs. (37)–(40), we are able to quantitatively reproduce the experimental results, see Figs. 2(a) and 2(b). The different current contributions (elastic, interference, and inelastic) are shown in Fig. 2 as well. As expected, the elastic term (green) gives the largest contribution followed by the interference term (yellow) and then the inelastic term (purple). Although visible in both panels, this is best seen in the conductance spectrum [Fig. 2(b)]. The elastic term evolves smoothly retracing the nonconstant DOS. The most prominent feature in the differential conductance is a big step near zero bias voltage, which originates from the interference term. This is due to the rather strong spin polarization in the tip, which transfers its polarization onto the spin system (see discussion in Appendix B). It is worth stressing that we find a very high spin polarization ($|p| = 0.8$), which may explain the difficulty in preparing ESR-active tips. Let us also say that, although not featureless, the inelastic term only gives a small contribution

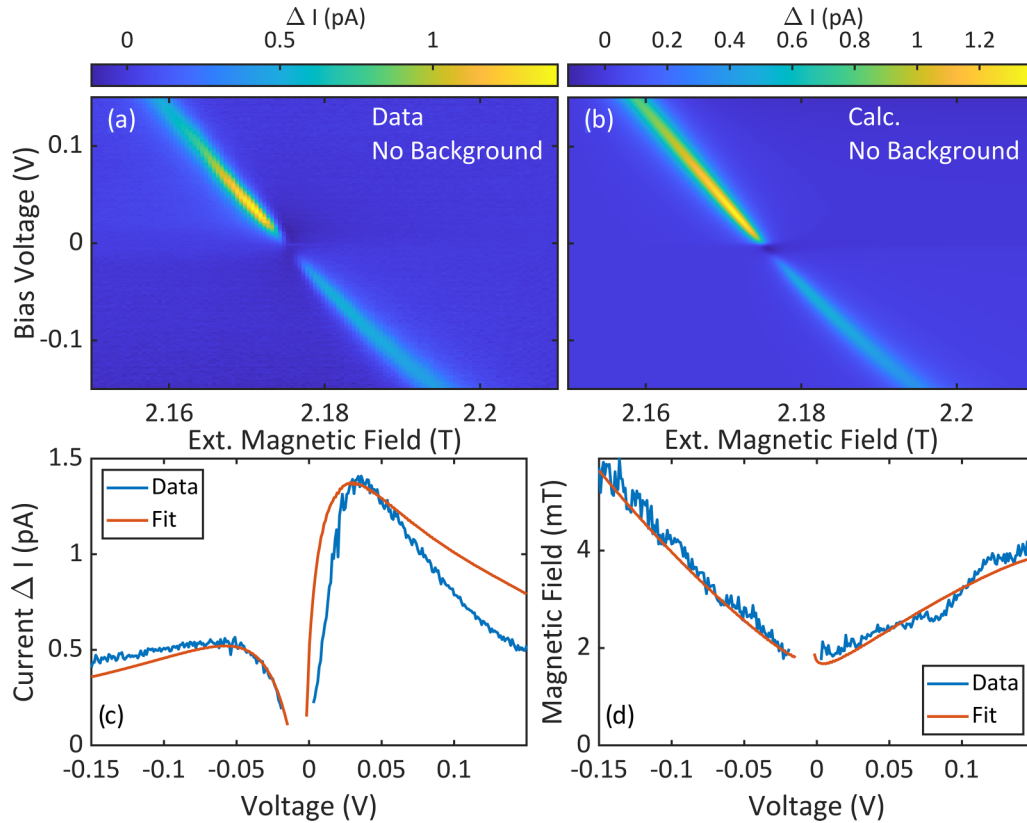


FIG. 3. Analyzing the ESR peak shape: (a) Measured ESR signal as function of bias voltage and external magnetic field at a constant frequency (61 GHz) with the off resonance background subtracted from Fig. 1(c). (b) Calculated ESR signal with the off resonance background subtracted. The parameters are chosen for a best fit to the data in (a). Comparison of the ESR peak height (c) and ESR peak width (d) extracted from the data in (a) and (b). The fit parameters have been determined from panels (c) and (d).

to the overall signal. From this fit we obtain most of the parameters of the model except those related to the microwaves. The values of those parameters are summarized in Table I.

B. ESR spectra

The ESR calculation in Fig. 1(d) has been done using the parameters extracted from the data without microwaves in Fig. 2. The relaxation and decoherence rates determining the spin dynamics can be readily calculated from the extracted parameters in Fig. 2(a) and are displayed in Fig. 2(c). The corresponding timescales are plotted in Fig. 2(d). For this calculation, we have to include the microwave frequency as an input parameter, which we set to 61 GHz here. The remaining parameters can be extracted from measurements with microwaves. The peak positions ω_{\max} , B_{\max} are extracted as function of bias voltage. The functional dependence of the peak position on the bias voltage is due to the electric field in the tunnel junction induced by the bias voltage, which is discussed elsewhere and will not be detailed here [21]. The peak positions are used as input parameters in the calculations.

For the subsequent analysis, we subtract the off-resonance background in the measured and calculated data in Figs. 1(c) and 1(d), respectively. We take a slice as function of bias voltage at a constant magnetic field that does not show any resonance signal and subtract it from every other slice in the

data set. The corrected measured and calculated data is shown in Figs. 3(a) and 3(b), respectively, with a smooth background demonstrating that the subtracted off-resonance background is independent of magnetic field. With the ESR peak positions known, we can extract the peak height and the peak width (full width at half) from the corrected data in Fig. 3(a), which are shown in Figs. 3(c) and 3(d), respectively. The data is shown in blue, while the fit is shown in red. The only free parameters in this fit are the intrinsic coherence rate γ_0 , which is mostly given by the coupling to the substrate, as well as the microwave amplitude Ω (Rabi frequency), that excites the spin system. Their values are given in Table I. We find that all parameters have more or less impact on all different quantities, but some quantities are particularly influenced by certain parameters, which allows us to determine their values rather precisely. The impact is summarized in Table II.

The dynamics of the system due to the tunneling current is entirely determined by the parameters that were already independently determined by the reference spectrum. We find excellent agreement between the data and the model calculations for the peak height and the peak width in Figs. 3(c) and 3(d). The only deviation we find is in the peak height for voltages larger than about 60 mV, which could be resolved by making some parameters voltage dependent. However, for the proof of principle here, we conclude that we have good agreement between data and theory. The corresponding relaxation

TABLE II. Impact of model parameter summary of the parameters used in the modeling and their impact on different measured quantities. Every parameter has a rather unique impact on one feature of the different measured quantities. This allows for a rather consistent fit, which little interdependence between fit parameters.

Parameter	Impact
p	dI/dV (inelastic step height)
τ_0	dI/dV (overall scaling)
$\tau_{1,2}/\tau_0$	dI/dV (overall slope)
λ	dI/dV (inelastic step height vs. overall scaling)
$\hbar\Gamma_0$	dI/dV (step width)
ω_{\max}, B_{\max}	Map (ESR peak position)
V_{ac}	Background (scaling)
$\hbar\Omega$	ESR peak height (overall scaling)
$\hbar\gamma_0$	ESR peak width (zero bias voltage offset)
θ	ESR spectrum near zero bias

rates $\Gamma_{a \rightarrow b}$ and $\Gamma_{b \rightarrow a}$ as well as the decoherence rate Γ_{ab}^{ad} are displayed in Fig. 2(c). Notice that the impact of the tunneling current is minimized at zero bias voltage.

As before, we separate the contributions to the ESR signal into the three tunneling channels. The elastic current channel

does not interact with the spin system and, will therefore not contribute to the ESR signal. However, the elastic current channel is influenced by the microwave, so that it will contribute to the off-resonance background. The interference term carries the majority of the ESR signal as can be seen in Fig. 4(a). The background in the interference term is relatively smooth apart from a small step at zero bias voltage. The inelastic term contributes mostly to the off-resonance background with a sizable feature at zero bias voltage as shown in Fig. 4(b). However, the inelastic term also carries part of the ESR signal. This ESR signal is substantially smaller than in the interference term, but it cannot be neglected in the data analysis if quantitative agreement is to be achieved.

Another important parameter to be determined is the microwave amplitude V_{ac} for the tunneling current. This can best be extracted from the off-resonance background, which is shown in Fig. 4(c). The nontrivial behavior of the off-resonance background is an indication of a nonconstant DOS. A constant/linear/quadratic DOS results in a zero/constant/linear offset in the off-resonance background. The sharp dip at zero bias voltage is due to the step feature in the interference term [cf. Fig. 2(b)]. The smaller wavy features are higher order details in the DOS, which are not captured by the quadratic approximation in Eq. (49). The behavior

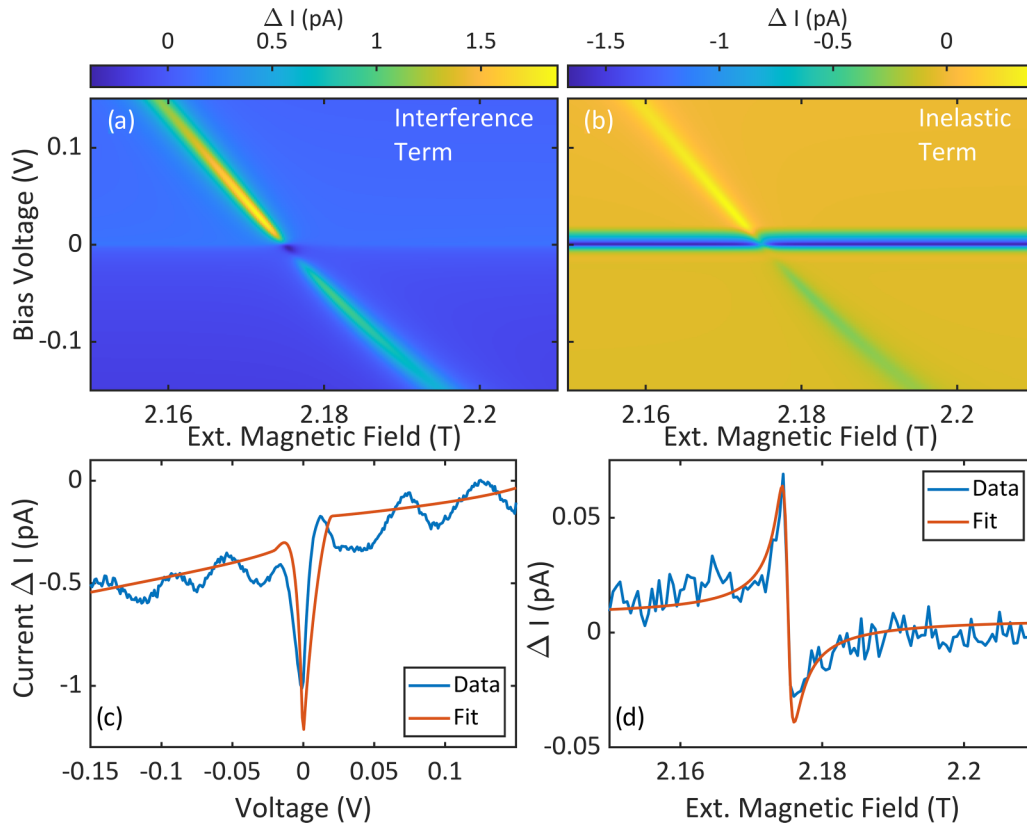


FIG. 4. Components of the ESR signal. Contribution of the interference term (a) and the inelastic term (b) to the ESR signal in Fig. 1(d). Most of the ESR signal is carried by the interference term. Note that there is a small contribution from the inelastic term to the ESR signal. (c) Off resonance background taken from Figs. 1(c) and 1(d) for the experimental and the calculated data, respectively. The wavy modulation in the data is due to the microwave interaction with small modulations in the DOS of the leads. (d) The homodyne signal near zero bias voltage at $V_{\text{bias}} = -2.713$ mV. The angle between the tip spin and the spin system is $\theta = 4.5^\circ$. The calculated spectrum was offset by 10 fA to compensate for slight differences in the background signal.

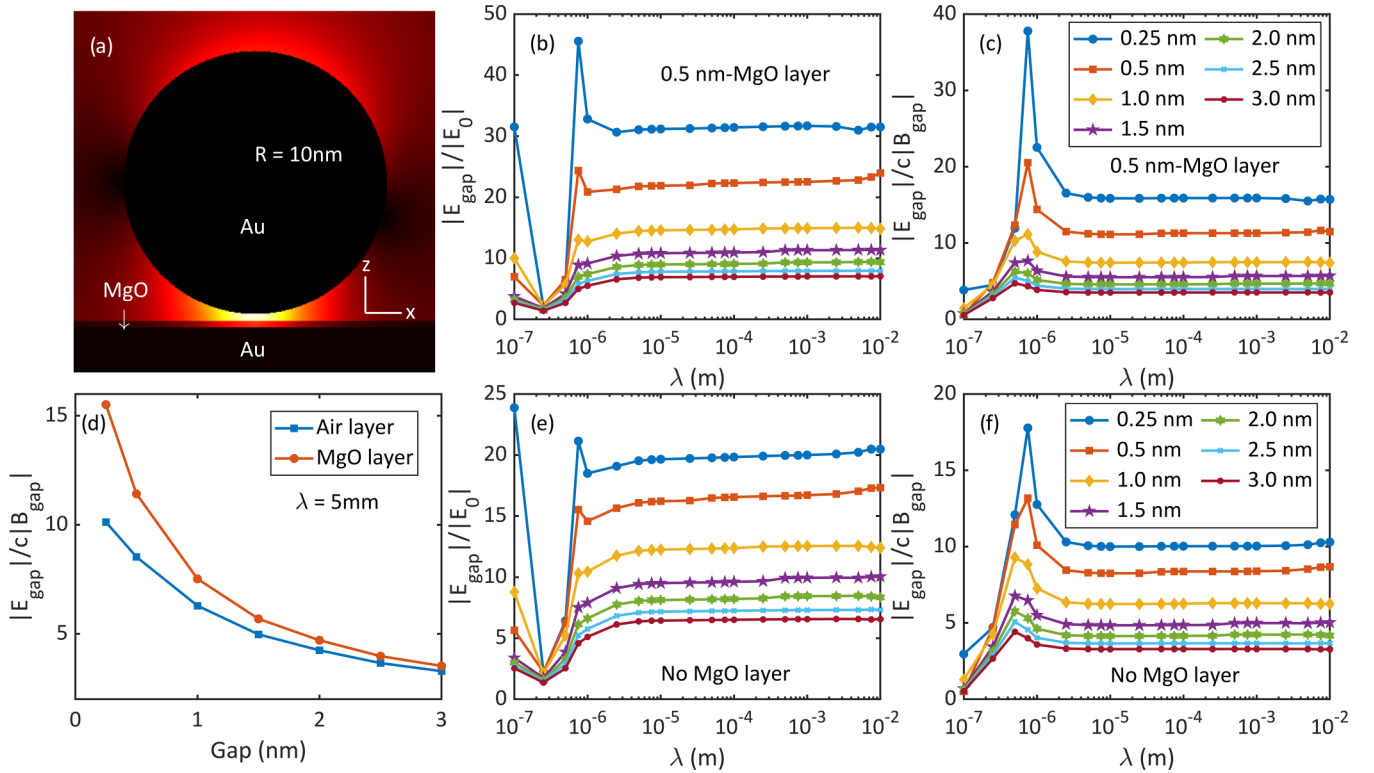


FIG. 5. Electromagnetic simulations: (a) System considered in the electromagnetic simulations in which a metallic sphere is placed above a metallic substrate that features an 0.5-nm-thick MgO layer on top. The metal is assumed to be gold and the sphere radius is 10 nm. In our simulations we vary the gap size (sphere-MgO distance) between 0.25 and 3 nm. In this panel we show the spatial distribution of the electric field amplitude in linear scale, from minimum (black) to maximum (yellow), when the system is illuminated with a plane wave with a wavelength of 5 mm, polarization along the z axis and incoming from the negative x direction. (b) Field enhancement ratio $|E_{\text{gap}}|/|E_0|$ as a function of the radiation wavelength for the system shown in panel (a). Here, $|E_{\text{gap}}|$ is evaluated in the middle of the gap region. The different curves correspond to different values of gap size, as indicated in the legend of (c). (c) The corresponding results for the field ratio $|E_{\text{gap}}|/(c|B_{\text{gap}}|)$. (d) The field ratio as a function of the gap size for the cases with and without a MgO layer for a wavelength of 5 mm. [(e) and (f)] The same as in (b) and (c), but replacing the MgO layer by air. The gap size indicated in the legend of panel (f) is measured from the top of the 0.5-nm-thick air layer to the gold sphere to make a fair comparison with the results of (b) and (c).

of the off-resonance background also depends sensitively on the microwave amplitude, so that we can extract a value of $V_{\text{ac}} = 19.9$ mV.

Near zero bias voltage, a small asymmetric ESR peak remains, which is attributed to homodyne detection [6,8,13,14]. The presence of this small signal, which can be seen in Fig. 4(d), indicates a finite angle between the tip spin and the spin system resulting in a homodyne signal (cf. Sec. III C). To determine this angle, we identify the zero crossing of the ESR peak height from the calculated spectra at $V_{\text{bias}} = -2.713$ mV. The corresponding ESR signal is shown in Fig. 4(d). We then set the angle to $\theta = 4.5^\circ$ to fit to the data showing excellent agreement. We thus find an overall consistent model that quantitatively explains the ESR features and the background signal over several orders of magnitude in the tunneling current.

VI. WHAT DRIVES THE TRANSITIONS?

Our theory has been able to clarify many basic questions so far, but we still need to address the most important question in this field: what drives the transitions between electronic

states? It is somehow surprising that an all-electric ESR can work at all. After all, the electric field should not couple to the spin (electric dipole transitions are forbidden due to selection rules). It has been argued that the ac magnetic field that accompanies the oscillating electric field is not strong enough to induce the transitions between the spin states [28]. For this reason, a plethora of alternative mechanisms have been proposed [3,14,23–27], but the community has not yet reached a consensus. In the context of our experiments, in which microwaves are supplied by an antenna radiating into the vacuum towards the tunnel junctions, the question boils down to whether the ac magnetic field at the junction is sufficiently intense to justify the value of the Rabi frequency Ω that we have deduced from our fits to the experimental results. To shed light on this question, we have carried out classical electromagnetic simulations using the frequency-domain, finite-element solver implemented in Comsol Multiphysics. Mimicking recent models for STM luminescence [57], we simulate our experiments through an Au nanocavity (with a radius of 10 nm) separated by a gap d from a Au surface, which features a 0.5-nm-thick MgO layer on top, see Fig. 5(a). To model Au, we used a permittivity obtained from a Drude

multi-Lorentz fit to the experimental data of Ref. [58]. Let us stress that the choice of the metal here is simply for convenience as all metals behave very similarly in the microwave region. In order to determine the electric and magnetic fields in the junction region, we have simulated the propagation of a plane wave incoming along the x direction [cf. Fig. 5(a)] with a wavelength λ , a far-field magnitude of the electric field equal to $|E_0|$, and with a polarization along the axis of the junction, which is the z direction in Fig. 5(a). The figure shows the electric field distribution for a gap of $d = 0.5$ nm, a 0.5-nm-thick MgO layer, and an incoming wave of $\lambda = 5$ mm wavelength (~ 61 GHz). Notice that the electric field is enhanced in the gap region. It is basically constant across the gap region and barely penetrates inside the metallic regions.

To characterize the intensity of the electromagnetic fields in the junction region, we present in Figs. 5(b)–5(f) results for the ratios $|E_{\text{gap}}|/|E_0|$ and $|E_{\text{gap}}|/(c|B_{\text{gap}}|)$, where $|E_{\text{gap}}|$ and $|B_{\text{gap}}|$ are the magnitudes of the electric and magnetic field, respectively, evaluated half way from the nanocavity and the MgO layer (c is the speed of light). Moreover, to understand the role of the MgO substrate, we also present in Figs. 5(d)–5(f) results without the MgO layer, which is simply replaced by an air layer of the same thickness. Let us first discuss the results shown in Figs. 5(b) and 5(e), which shows the electric field enhancement with and without the MgO layer as a function of the radiation wavelength ranging from UHV light to the microwave range. The wavelength in our experiments is ~ 5 mm, but to connect with field enhancements in other contexts like nanoplasmonics, we present several orders of magnitude in λ . The different curves correspond to different values of the gap size d , which are listed in Figs. 5(c) and 5(f). Notice that for the smallest gaps and microwave wavelengths, the electric field is locally enhanced at the junction region by a factor between 10 and 30 depending on the precise value of the gap and the presence or absence of the MgO layer. This enhancement in the microwave region is due to the well-known lightning-rod effect and has nothing to do with the excitation of local plasmons, which do not exist in this region of the electromagnetic spectrum. Indeed, for all gap sizes, the field enhancement is maximum in the near-infrared and the red region of the optical window (600–900 nm). At these wavelengths, the structure supports bright localized plasmons, which couple efficiently to the incoming radiation. The local electric field enhancement is progressively reduced as the gap size increases. Furthermore, the presence of the MgO layer increases the field enhancement.

In Figs. 5(c) and 5(f), we show the corresponding results for the ratio $|E_{\text{gap}}|/(c|B_{\text{gap}}|)$. This ratio is equal to one in the far field and it increases in the gap region up to an order of magnitude for small gaps in the microwave region, meaning that the magnetic field is relatively reduced with respect to the electric field. Going back to our relevant wavelength of about 5 mm, we summarize the decrease of the ratio $|E_{\text{gap}}|/(c|B_{\text{gap}}|)$ as the gap increases in Fig. 5(d) for the cases with and without the MgO layer. Notice that the presence of a layer of the MgO dielectrics leads to a more rapid decrease of the field ratio with increasing gap size.

Let us now use these simulations to connect with the results of Sec. V. We note that in our experiments we do not have

access to the values of the fields in the far-field region, i.e., we do not know $|E_0|$ in our experiments. However, we can use the fitted value for V_{ac} to get an estimate for the magnitude of the electric field in the junction and then use the results of Fig. 5 to obtain the value of the magnetic field that determines the Rabi frequency. We can estimate the magnitude of the electric field in the gap region as: $|E_{\text{gap}}| \approx V_{\text{ac}}/d$. We have checked that in the microwave regime, this simple estimate reproduces very well the rigorous result obtained integrating the profile of the z component of the electric field along the axis of the junction. Now, assuming a gap of $d = 2$ nm (to account for the tiny field penetration in the metallic regions) and using $V_{\text{ac}} = 19.9$ mV, we obtain $|E_{\text{gap}}| \sim 10^7$ V/m. Then, using a typical value of $|E_{\text{gap}}|/(c|B_{\text{gap}}|) \sim 5$ for the field ratio at the junction, we can estimate that $|B_{\text{gap}}| \sim 6$ mT. This value has to be compared with the magnetic field deduced from the Rabi frequency: $\Omega = \mu_B |B_{\text{gap}}|/\hbar$, where we assume that the g -factor is equal to two for our spin-1/2 system. Note that the relevant magnetic field component relevant is in the xy -plane (perpendicular to the static magnetic field), which is precisely the one that is reported in the simulations of Fig. 5. Using $\hbar\Omega = 29$ neV, we obtain $|B_{\text{gap}}| \sim 0.6$ mT, which is smaller than the estimate above that was obtained using ideal conditions in terms of propagation direction and polarization. Thus we conclude from these arguments that in our setup, the ESR transitions can be attributed to the ac magnetic field of the microwave radiation.

VII. DISCUSSION AND CONCLUSIONS

The discussion of the previous section applies to situations in which the microwaves are supplied via a nearby antenna radiating into vacuum. It would be highly desirable to carry out a similar analysis to clarify what happens in those cases in which an alternating electric field is fed directly to the tip, like in the original experiment [3]. In those cases, we have no statement about the driving of the transitions and cannot exclude other proposed mechanisms. However, we emphasize here that our theory applies irrespective of how the spin system is driven. Furthermore, a number of theoretical works have treated the ESR-STM theory recently [25–27,51,59], with Refs. [25–27] being closest in spirit to our work albeit with an excitation mechanism employing a time-dependent variation of the tunnel barrier induced by the alternating electric driving field. The most notable differences to the previous theories are that we went beyond the small amplitude approximation for the microwave, we allowed for a nonconstant density of states, and we included the background current to achieve the best possible quantitative agreement with the experimental data.

In summary, we have presented a comprehensive theory of ESR-STM based on a combination of nonequilibrium Green's function techniques for the calculation of the current and quantum master equations for the description of the spin dynamics. Our theory naturally includes the interplay between the microwave field, the spin dynamics and the tunneling electrons. It accounts not only for the ESR signals but also for the background current that contains critical information about the underlying physics. This theory can be applied to any spin system and its validity has been established here with a comparison with experimental results for a well-known

spin-1/2 system (TiH on MgO). The quantitative agreement between theory and experiment was found over many orders of magnitude of the tunneling current and in a consistent manner, such that most model parameters were determined with reference spectra in the absence of microwaves. Such a quantitative agreement allowed us to unambiguously extract the relevant times scales (relaxation and decoherence times). On more general grounds, our theory clarifies what the ESR-STM spectroscopy measures by rigorously justifying some of the heuristic formulas that have been customarily employed to analyze ESR signals. This rigorous analysis has allowed us, in particular, to determine the degree of spin polarization of the STM tip in our experiments, which is surprisingly high ($\sim 80\%$) and could explain the difficulties in fabricating ESR-active tips. In addition, we have corroborated how the asymmetry often observed in ESR spectra is due to homodyne detection, i.e., to the coupling of the spin precession and the microwaves when the spins are not aligned. Moreover, with the help of first-principle electromagnetic simulations we have shown for the scenarios, in which the microwaves are supplied by an antenna, the origin of the spin transition can be attributed to the ac magnetic field in the junction region generated by the radiation field. Furthermore, our theory is constructed in a modular way such that it can be readily generalized in many different ways: more complex spin systems, inclusion of hyperfine interactions, analysis of pump-probe experiments, including other environments (such as dynamical Coulomb blockade), the analysis of the interplay between ESR and superconductivity, etc. In this regard, we believe that the theory presented here will help to expand the ESR-STM capabilities in the coming years.

ACKNOWLEDGMENTS

The authors would like to thank Susanne Baumann, Andreas Heinrich, Klaus Kern, Sebastian Loth, Sander Otte, Aparajita Singha, and Markus Ternes for fruitful discussions. We are grateful to the European Research Council (ERC) for their financial support. This study was funded in part by the ERC Consolidator Grant AbsoluteSpin (Grant No. 681164). S.P. acknowledges the support from the Condensed Matter Physics Center (IFIMAC) through an IFIMAC's Master Grants for 2022-2023. A.I.F.-D. acknowledges funding from the Spanish Ministry of Science, Innovation and Universities through Grants No. PID2021-126964OB-I00 and No. ED2021-130552B-C21, as well as the European Union's Horizon Programme through Grant No. 101070700 (MIRAQLS). J.C.C. thanks the Spanish Ministry of Science and Innovation (Grant No. PID2020-114880GB-I00) for financial support and the Deutsche Forschungsgemeinschaft (DFG) via

SFB 1432 for sponsoring his stay at the University of Konstanz as a Mercator Fellow.

APPENDIX A: EXPERIMENTAL METHODS

Experiments were done using a commercial Unisoku USM-1300 STM equipped with high-frequency cabling and an antenna. The high-frequency setup allows for driving ESR signals between 60 to 100 GHz [54]. We cleaned a silver Ag(100) single crystal in ultrahigh vacuum (UHV) through several cycles of Ar⁺ ion sputtering at 5 kV and annealing at 820 K. Double layer MgO was grown on the clean silver surface by simultaneous evaporation of Mg onto the sample surface, leaking of O₂ into the UHV space, and heating of the silver substrate. After the MgO growth, we deposited single Fe and Ti atoms onto the surface using electron beam evaporators. Furthermore, the sample was kept below 16 K during Fe and Ti deposition to ensure that the atomic species did not form clusters on the surface. The Ti species naturally hydrate due to the residual hydrogen gas found in the UHV space [53]. To create ESR sensitive tips we picked up between one and ten Fe atoms [3]. All measurements were done with a setpoint current of 100 pA at a setpoint voltage of 100 mV.

APPENDIX B: MORE ON THE SPIN 1/2 SYSTEM

In this Appendix, we elaborate on the case of a spin-1/2 system and provide some analytical results for more in-depth insight. To proceed, we shall assume that the electrodes' DOS are energy-independent with a spin polarization p and that the bias voltage is the dominant energy scale, i.e., $\hbar\omega_0 \equiv eV \gg k_B T, \hbar\omega_{ba}$. Within these approximations the relaxation and decoherence rates (and the corresponding characteristic times T_1 and T_2) are given by

$$\Gamma_{a \rightarrow b} = \frac{\lambda^2 \tau_0}{\pi} \frac{1 + \text{sgn}(\omega_0)p}{2} |\omega_0|, \quad (\text{B1})$$

$$\Gamma_{b \rightarrow a} = \frac{\lambda^2 \tau_0}{\pi} \frac{1 - \text{sgn}(\omega_0)p}{2} |\omega_0| + \Gamma_0, \quad (\text{B2})$$

$$\Gamma_{ab}^{\text{ad}} = \frac{\lambda^2 \tau_0}{2\pi} |\omega_0| + \gamma_0, \quad (\text{B3})$$

$$\Gamma = \frac{1}{T_1} = \frac{\lambda^2 \tau_0}{\pi} |\omega_0| + \Gamma_0, \quad (\text{B4})$$

$$\gamma = \frac{1}{T_2} = \frac{\lambda^2 \tau_0}{\pi} |\omega_0| + \frac{\Gamma_0}{2} + \gamma_0, \quad (\text{B5})$$

$$\Gamma' = \Gamma_0 - \frac{\lambda^2 \tau_0}{\pi} p \omega_0. \quad (\text{B6})$$

With these expressions we can obtain the different elements of the stationary density matrix [cf. Eq. (33)], which adopt the form

$$\rho_{aa} = \frac{(|\tilde{\omega}| + \tilde{\gamma}_0)\Omega^2 + [(1 - \text{sgn}(\tilde{\omega})p)|\tilde{\omega}| + 2\Gamma_0][\delta^2 + (|\tilde{\omega}| + \tilde{\gamma}_0)^2]}{2(|\tilde{\omega}| + \tilde{\gamma}_0)\Omega^2 + 2[|\tilde{\omega}| + \Gamma_0][\delta^2 + (|\tilde{\omega}| + \tilde{\gamma}_0)^2]}, \quad (\text{B7})$$

$$\rho_{bb} = \frac{(|\tilde{\omega}| + \tilde{\gamma}_0)\Omega^2 + 2[(1 + \text{sgn}(\tilde{\omega})p)|\tilde{\omega}| + 2\Gamma_0][\delta^2 + (|\tilde{\omega}| + \tilde{\gamma}_0)^2]}{2(|\tilde{\omega}| + \tilde{\gamma}_0)\Omega^2 + 2[|\tilde{\omega}| + \Gamma_0][\delta^2 + (|\tilde{\omega}| + \tilde{\gamma}_0)^2]}, \quad (\text{B8})$$

$$\tilde{\rho}_{ab} = \frac{\Omega(\Gamma_0 - p\tilde{\omega})[\delta + i(\tilde{\gamma}_0 + |\tilde{\omega}|)]}{2(|\tilde{\omega}| + \tilde{\gamma}_0)\Omega^2 + 2[|\tilde{\omega}| + \Gamma_0][\delta^2 + (|\tilde{\omega}| + \tilde{\gamma}_0)^2]}. \quad (\text{B9})$$

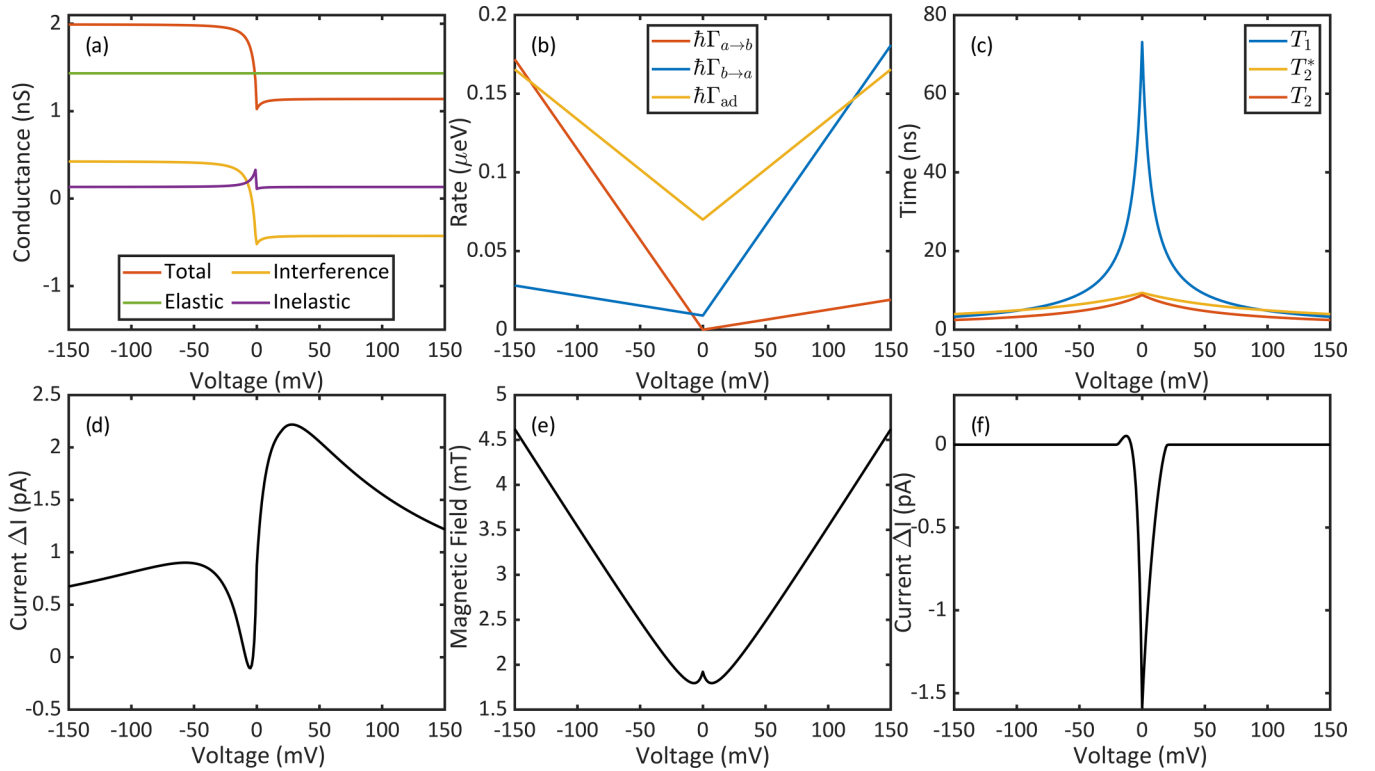


FIG. 6. Analytical results for the spin-1/2 system: (a) Conductance in the absence of microwaves. The different contributions are the elastic term (green), the interference term (yellow), the inelastic term (purple), and the total conductance (red). (b) The different rates determining the dynamics of the two-level system. (c) The corresponding relaxation and decoherence times. (d) ESR peak width. (e) ESR peak width. (f) Off-resonant background current. The parameters used to compute these results were those reported in Table I.

Here, we have defined $\tilde{\omega} = \lambda^2 \tau_0 \omega_0 / \pi$ and $\tilde{\gamma}_0 = \Gamma_0 / 2 + \gamma_0$. It is interesting to notice that in the limit of large voltages, the stationary density matrix reduces to

$$\rho(V \rightarrow \pm\infty) = \frac{1 - \text{sgn}(V)p\sigma^z}{2}. \quad (\text{B10})$$

This means that for sufficiently high bias voltages, the polarization of the spin system follows the spin polarization of the tip. In this limit, the expectation value of the magnetization in the z -direction becomes $\langle S^z \rangle = \mp p \hbar / 2$, depending on the sign of the bias. This corroborates the observation that the thermal excitation of the spin system for $k_B T > \hbar \omega_{ba}$, reducing the ESR signal becomes irrelevant at high enough bias voltages making it still observable at higher temperatures [60].

With these expressions, we can compute the current. First, the elastic current of Eq. (38) and related quantities in the absence of microwaves are given by

$$I_{\text{el}}^{\sigma}(V) = G_0 \tau_0 \frac{1 \pm p}{2} V, \quad (\text{B11})$$

$$I_{\text{el}}(V) = I_{\text{el}}^{\uparrow}(V) + I_{\text{el}}^{\downarrow}(V) = G_0 \tau_0 V, \quad (\text{B12})$$

$$I_{\text{pol}}(V) = I_{\text{el}}^{\uparrow}(V) - I_{\text{el}}^{\downarrow}(V) = G_0 \tau_0 p V, \quad (\text{B13})$$

where $G_0 = 2e^2/h$ is the conductance quantum. The interference term, see Eq. (39), can be written as

$$I_{\text{int}}(V) = \lambda G_0 \tau_0 p V (\rho_{aa} - \rho_{bb}), \quad (\text{B14})$$

while the inelastic current, see Eq. (40), adopts the form

$$I_{\text{inel}}(V) = \frac{3\lambda^2 G_0 \tau_0}{4} V + \frac{\lambda^2 G_0 \tau_0 p}{2} \tilde{V} (\rho_{aa} - \rho_{bb}), \quad (\text{B15})$$

where $\tilde{V} \equiv \sum_n J_n^2(\alpha) |V + n \hbar \omega_r / e|$. Thus the total dark current within this approximation is given by

$$I^{\text{dark}}(V) = G_0 \tau_0 \left[\left(1 + \frac{3\lambda^2}{4} + \frac{\lambda p \Gamma'}{\Gamma} \right) V + \frac{\lambda^2 p \Gamma'}{2\Gamma} |V| \right]. \quad (\text{B16})$$

The previous analytical results for the conductance as well as for the relaxation and decoherence rates and timescales are illustrated in Figs. 6(a)–6(c).

Both the interference and inelastic terms contribute to the ESR lineshape that is given by Eq. (41) where the peak height can be expressed as

$$I_{\text{peak}}(V) = -\lambda G_0 \tau_0 p \left(V + \frac{\lambda \tilde{V}}{2} \right) \frac{\Gamma_0 - p \tilde{\omega}}{\Gamma_0 + |\tilde{\omega}|} \times \frac{\Omega^2}{(|\tilde{\omega}| + \tilde{\gamma}_0)(|\tilde{\omega}| + \Gamma_0) + \Omega^2}, \quad (\text{B17})$$

while the corresponding linewidth adopts the form

$$\mathcal{W}(V) = (|\tilde{\omega}| + \tilde{\gamma}_0) \sqrt{1 + \frac{\Omega^2}{(|\tilde{\omega}| + \tilde{\gamma}_0)(|\tilde{\omega}| + \Gamma_0)}}. \quad (\text{B18})$$

These expressions qualitatively reproduce the nonmonotonic behavior of the peak height shown in Fig. 3(c) and the approximate linear dependence of the linewidth with the bias

voltage, see Fig. 3(d). This is illustrated in Figs. 6(d) and 6(e). However, for a quantitative agreement with our experimental results the energy dependence of the DOS cannot be ignored and the full theory described in the main text has to be used.

It is worth mentioning that within the approximations used in this Appendix the background or off-resonant current is solely due to the inelastic term and it is given by

$$I_{\text{background}}(V) = \frac{\lambda^2 G_0 \tau_0 p \Gamma'}{2 \Gamma} (\tilde{V} - |V|). \quad (\text{B19})$$

This result is illustrated in Fig. 6(f).

Finally, it is also interesting to address the homodyne detection discussed in Sec. III C. Assuming a constant DOS, Eq. (45) becomes

$$I_{\text{int}}(V, \alpha) = \lambda G_0 \tau_0 p V (\rho_{aa} - \rho_{bb}) \cos \theta + \lambda G_0 \tau_0 p V_{\text{ac}} \text{Re}\{\tilde{\rho}_{ba}\} \sin \theta. \quad (\text{B20})$$

As discussed in Sec. III C, the second term is responsible for the asymmetry in the ESR spectra.

-
- [1] A. Abragam and B. Bleaney, *Electron Paramagnetic Resonance of Transition Ions* (Oxford Classic Texts in the Physical Sciences, Oxford, 2012).
- [2] R. M. Fratila and A. H. Velders, Small-volume nuclear magnetic resonance spectroscopy, *Annu. Rev. Anal. Chem.* **4**, 227 (2011).
- [3] S. Baumann, W. Paul, T. Choi, C. P. Lutz, A. Ardavan, and A. J. Heinrich, Electron paramagnetic resonance of individual atoms on a surface, *Science* **350**, 417 (2015).
- [4] F. D. Natterer, K. Yang, W. Paul, P. Willke, T. Choi, T. Greber, A. J. Heinrich, and C. P. Lutz, Reading and writing single-atom magnets, *Nature (London)* **543**, 226 (2017).
- [5] T. Choi, W. Paul, S. Rolf-Pissarczyk, A. J. MacDonald, F. D. Natterer, K. Yang, P. Willke, C. P. Lutz, and A. J. Heinrich, Atomic-scale sensing of the magnetic dipolar field from single atoms, *Nat. Nanotechnol.* **12**, 420 (2017).
- [6] P. Willke, W. Paul, F. D. Natterer, K. Yang, Y. Bae, T. Choi, J. Fernández-Rossier, A. J. Heinrich, and C. P. Lutz, Probing quantum coherence in single-atom electron spin resonance, *Sci. Adv.* **4**, eaaq1543 (2018).
- [7] P. Willke, Y. Bae, K. Yang, J. L. Lado, A. Ferrón, T. Choi, A. Ardavan, J. Fernández-Rossier, A. J. Heinrich, and C. P. Lutz, Hyperfine interaction of individual atoms on a surface, *Science* **362**, 336 (2018).
- [8] Y. Bae, K. Yang, P. Willke, T. Choi, A. J. Heinrich, and C. P. Lutz, Enhanced quantum coherence in exchange coupled spins via singlet-triplet transitions, *Sci. Adv.* **4**, eaau4159 (2018).
- [9] K. Yang, P. Willke, Y. Bae, A. Ferrón, J. L. Lado, A. Ardavan, J. Fernández-Rossier, A. J. Heinrich, and C. P. Lutz, Electrically controlled nuclear polarization of individual atoms, *Nat. Nanotechnol.* **13**, 1120 (2018).
- [10] P. Willke, A. Singha, X. Zhang, T. Esat, C. P. Lutz, A. J. Heinrich, and T. Choi, Tuning single-atom electron spin resonance in a vector magnetic field, *Nano Lett.* **19**, 8201 (2019).
- [11] P. Willke, K. Yang, Y. Bae, A. J. Heinrich, and C. P. Lutz, Magnetic resonance imaging of single atoms on a surface, *Nat. Phys.* **15**, 1005 (2019).
- [12] K. Yang, W. Paul, F. D. Natterer, J. L. Lado, Y. Bae, P. Willke, T. Choi, A. Ferrón, J. Fernández-Rossier, A. J. Heinrich, and C. P. Lutz, Tuning the exchange bias on a single atom from 1 mT to 10 T, *Phys. Rev. Lett.* **122**, 227203 (2019).
- [13] K. Yang, W. Paul, S.-H. Phark, P. Willke, Y. Bae, T. Choi, T. Esat, A. Ardavan, A. J. Heinrich, and C. P. Lutz, Coherent spin manipulation of individual atoms on a surface, *Science* **366**, 509 (2019).
- [14] T. S. Seifert, S. Kovarik, D. M. Juraschek, N. A. Spaldin, P. Gambardella, and S. Stepanow, Longitudinal and transverse electron paramagnetic resonance in a scanning tunneling microscope, *Sci. Adv.* **6**, eabc5511 (2020).
- [15] W. M. J. van Weerdenburg, M. Steinbrecher, N. P. E. van Mullekom, J. W. Gerritsen, H. von Allwörden, F. D. Natterer, and A. A. Khajetoorians, A scanning tunneling microscope capable of electron spin resonance and pump-probe spectroscopy at mK temperature and in vector magnetic field, *Rev. Sci. Instrum.* **92**, 033906 (2021).
- [16] M. Steinbrecher, W. M. J. van Weerdenburg, E. F. Walraven, N. P. E. van Mullekom, J. W. Gerritsen, F. D. Natterer, D. I. Badrtdinov, A. N. Rudenko, V. V. Mazurenko, M. I. Katsnelson, A. van der Avoird, G. C. Groenenboom, and A. A. Khajetoorians, Quantifying the interplay between fine structure and geometry of an individual molecule on a surface, *Phys. Rev. B* **103**, 155405 (2021).
- [17] L. M. Veldman, L. Farinacci, R. Rejali, R. Broekhoven, J. Gobeil, D. Coffey, M. Ternes, and A. F. Otte, Free coherent evolution of a coupled atomic spin system initialized by electron scattering, *Science* **372**, 964 (2021).
- [18] J. Kim, K. Noh, Y. Chen, F. Donati, A. J. Heinrich, C. Wolf, and Y. Bae, Anisotropic hyperfine interaction of surface-adsorbed single atoms, *Nano Lett.* **22**, 9766 (2022).
- [19] S. Kovarik, R. Robles, R. Schlitz, T. S. Seifert, N. Lorente, P. Gambardella, and S. Stepanow, Electron paramagnetic resonance of alkali metal atoms and dimers on ultrathin mgo, *Nano Lett.* **22**, 4176 (2022).
- [20] X. Zhang, C. Wolf, Y. Wang, H. Aubin, T. Bilgeri, P. Willke, A. J. Heinrich, and T. Choi, Electron spin resonance of single iron phthalocyanine molecules and role of their non-localized spins in magnetic interactions, *Nat. Chem.* **14**, 59 (2022).
- [21] P. Kot, M. Ismail, R. Drost, J. Siebrecht, H. Huang, and C. R. Ast, Electric control of spin transitions at the atomic scale, *Nat. Commun.* **14**, 6612 (2023).
- [22] S.-h. Phark, Y. Chen, H. T. Bui, Y. Wang, M. Haze, J. Kim, Y. Bae, A. J. Heinrich, and C. Wolf, Double-resonance spectroscopy of coupled electron spins on a surface, *ACS Nano* **17**, 14144 (2023).
- [23] J. L. Lado, A. Ferrón, and J. Fernández-Rossier, Exchange mechanism for electron paramagnetic resonance of individual adatoms, *Phys. Rev. B* **96**, 205420 (2017).
- [24] A. Ferrón, S. A. Rodríguez, S. S. Gómez, J. L. Lado, and J. Fernández-Rossier, Single spin resonance driven by

- electric modulation of the g -factor anisotropy, *Phys. Rev. Res.* **1**, 033185 (2019).
- [25] J. Reina Gálvez, C. Wolf, F. Delgado, and N. Lorente, Cotunneling mechanism for all-electrical electron spin resonance of single adsorbed atoms, *Phys. Rev. B* **100**, 035411 (2019).
- [26] J. Reina-Gálvez, N. Lorente, F. Delgado, and L. Arrachea, All-electric electron spin resonance studied by means of Floquet quantum master equations, *Phys. Rev. B* **104**, 245435 (2021).
- [27] J. Reina-Gálvez, C. Wolf, and N. Lorente, Many-body nonequilibrium effects in all-electric electron spin resonance, *Phys. Rev. B* **107**, 235404 (2023).
- [28] F. Delgado and N. Lorente, A theoretical review on the single-impurity electron spin resonance on surfaces, *Prog. Surf. Sci.* **96**, 100625 (2021).
- [29] T. S. Seifert, S. Kovarik, P. Gambardella, and S. Stepanow, Accurate measurement of atomic magnetic moments by minimizing the tip magnetic field in STM-based electron paramagnetic resonance, *Phys. Rev. Res.* **3**, 043185 (2021).
- [30] S. A. Rodríguez, S. S. Gómez, J. Fernández-Rossier, and A. Ferrón, Optimizing tip-surface interactions in ESR-STM experiments, *Phys. Rev. B* **107**, 155406 (2023).
- [31] R. Kawaguchi, K. Hashimoto, T. Kakudate, K. Katoh, M. Yamashita, and T. Komeda, Spatially resolving electron spin resonance of π -radical in single-molecule magnet, *Nano Lett.* **23**, 213 (2023).
- [32] S. Loth, K. von Bergmann, M. Ternes, A. F. Otte, C. P. Lutz, and A. J. Heinrich, Controlling the state of quantum spins with electric currents, *Nat. Phys.* **6**, 340 (2010).
- [33] F. Delgado, J. J. Palacios, and J. Fernández-Rossier, Spin-transfer torque on a single magnetic adatom, *Phys. Rev. Lett.* **104**, 026601 (2010).
- [34] F. Delgado, Spin dynamics of current-driven single magnetic adatoms and molecules, *Phys. Rev. B* **82**, 134414 (2010).
- [35] J. Fernández-Rossier, Theory of single-spin inelastic tunneling spectroscopy, *Phys. Rev. Lett.* **102**, 256802 (2009).
- [36] J. Fransson, O. Eriksson, and A. V. Balatsky, Theory of spin-polarized scanning tunneling microscopy applied to local spins, *Phys. Rev. B* **81**, 115454 (2010).
- [37] M. Ternes, Spin excitations and correlations in scanning tunneling spectroscopy, *New J. Phys.* **17**, 063016 (2015).
- [38] F. Delgado and J. Fernández-Rossier, Spin decoherence of magnetic atoms on surfaces, *Prog. Surf. Sci.* **92**, 40 (2017).
- [39] J. C. Cuevas, J. Heurich, A. Martín-Rodero, A. Levy Yeyati, and G. Schön, Subharmonic Shapiro steps and assisted tunneling in superconducting point contacts, *Phys. Rev. Lett.* **88**, 157001 (2002).
- [40] J. C. Cuevas and E. Scheer, *Molecular Electronics: An Introduction To Theory And Experiment*, 2nd ed. (World Scientific, Singapore, 2017).
- [41] P. K. Tien and J. P. Gordon, Multiphoton process observed in the interaction of microwave fields with the tunneling between superconductor films, *Phys. Rev.* **129**, 647 (1963).
- [42] S. Kohler, J. Lehmann, and P. Hänggi, Driven quantum transport on the nanoscale, *Phys. Rep.* **406**, 379 (2005).
- [43] A. Roychowdhury, M. Dreyer, J. Anderson, C. Lobb, and F. Wellstood, Microwave photon-assisted incoherent Cooper-pair tunneling in a Josephson STM, *Phys. Rev. Appl.* **4**, 034011 (2015).
- [44] P. Kot, R. Drost, M. Uhl, J. Ankerhold, J. C. Cuevas, and C. R. Ast, Microwave-assisted tunneling and interference effects in superconducting junctions under fast driving signals, *Phys. Rev. B* **101**, 134507 (2020).
- [45] O. Peters, N. Bogdanoff, S. Acero González, L. Melischek, J. R. Simon, G. Reecht, C. B. Winkelmann, F. von Oppen, and K. J. Franke, Resonant Andreev reflections probed by photon-assisted tunnelling at the atomic scale, *Nat. Phys.* **16**, 1222 (2020).
- [46] J. Siebrecht, H. Huang, P. Kot, R. Drost, C. Padurariu, B. Kubala, J. Ankerhold, J. C. Cuevas, and C. R. Ast, Microwave excitation of atomic scale superconducting bound states, *Nat. Commun.* **14**, 6794 (2023).
- [47] A. Fetter and J. Walecka, *Quantum Theory of Many-Particle Systems*, Dover Books on Physics (Dover Publications, Mineola, New York, 2012).
- [48] C. Cohen-Tannoudji, J. Dupont-Roc, and G. Grynberg, *Atom-Photon Interactions: Basic Processes and Applications* (John Wiley & Sons, Ltd, New York, 1998).
- [49] H.-P. Breuer and F. Petruccione, *The Theory of Open Quantum Systems* (Oxford University Press, Oxford, 2007).
- [50] H. T. Dung, L. Knöll, and D.-G. Welsch, Resonant dipole-dipole interaction in the presence of dispersing and absorbing surroundings, *Phys. Rev. A* **66**, 063810 (2002).
- [51] G. Shavit, B. Horovitz, and M. Goldstein, Generalized open quantum system approach for the electron paramagnetic resonance of magnetic atoms, *Phys. Rev. B* **99**, 195433 (2019).
- [52] T. Nozaki, Y. Shiota, S. Miwa, S. Murakami, F. Bonell, S. Ishibashi, H. Kubota, K. Yakushiji, T. Saruya, A. Fukushima *et al.*, Electric-field-induced ferromagnetic resonance excitation in an ultrathin ferromagnetic metal layer, *Nat. Phys.* **8**, 491 (2012).
- [53] K. Yang, Y. Bae, W. Paul, F. D. Natterer, P. Willke, J. L. Lado, A. Ferrón, T. Choi, J. Fernández-Rossier, A. J. Heinrich, and C. P. Lutz, Engineering the eigenstates of coupled spin-1/2 atoms on a surface, *Phys. Rev. Lett.* **119**, 227206 (2017).
- [54] R. Drost, M. Uhl, P. Kot, J. Siebrecht, A. Schmid, J. Merkt, S. Wünsch, M. Siegel, O. Kieler, R. Kleiner, and C. R. Ast, Combining electron spin resonance spectroscopy with scanning tunneling microscopy at high magnetic fields, *Rev. Sci. Instrum.* **93**, 043705 (2022).
- [55] W. Paul, S. Baumann, C. P. Lutz, and A. J. Heinrich, Generation of constant-amplitude radio-frequency sweeps at a tunnel junction for spin resonance STM, *Rev. Sci. Instrum.* **87**, 074703 (2016).
- [56] F. D. Natterer, F. Patthey, T. Bilgeri, P. R. Forrester, N. Weiss, and H. Brune, Upgrade of a low-temperature scanning tunneling microscope for electron-spin resonance, *Rev. Sci. Instrum.* **90**, 013706 (2019).
- [57] A. Martín-Jiménez, A. I. Fernández-Domínguez, K. Lauwaet, D. Granados, R. Miranda, F. J. García-Vidal, and R. Otero, Unveiling the radiative local density of optical states of a plasmonic nanocavity by STM, *Nat. Commun.* **11**, 1021 (2020).

- [58] A. D. Rakić, A. B. Djurišić, J. M. Elazar, and M. L. Majewski, Optical properties of metallic films for vertical-cavity optoelectronic devices, *Appl. Opt.* **37**, 5271 (1998).
- [59] P. Berggren and J. Fransson, Electron paramagnetic resonance of single magnetic moment on a surface, *Sci. Rep.* **6**, 25584 (2016).
- [60] T. S. Seifert, S. Kovarik, C. Nistor, L. Persichetti, S. Stepanow, and P. Gambardella, Single-atom electron paramagnetic resonance in a scanning tunneling microscope driven by a radio-frequency antenna at 4 K, *Phys. Rev. Res.* **2**, 013032 (2020).